CIRCUIT MODELING OF SPINTRONIC DEVICES: A SPICE IMPLEMENTATION

A Thesis
Presented to
The Academic Faculty

By

Phillip Bonhomme Jr.

In Partial Fulfillment
of the Requirements for the Degree
Master of Science
in
Electrical and Computer Engineering

School of Electrical and Computer Engineering
Georgia Institute of Technology
May 2014

CIRCUIT MODELING OF SPINTRONIC DEVICES: A SPICE IMPLEMENTATION

Approved by:

Dr. Azad Naeemi, Advisor
Associate Professor, School of ECE
Georgia Institute of Technology

Dr. Saibal Mukhopadhyay
Associate Professor, School of ECE
Georgia Institute of Technology

Dr. Jeff Davis
Associate Professor, School of ECE
Georgia Institute of Technology

Date Approved: February 2014

ACKNOWLEDGMENT

Thanks to everyone that I've met along the way during my journey, especially to my Professor, Dr. Azad Naeemi

TABLE OF CONTENTS

LIST OF FIGURES

To my parents.

CHAPTER 1

INTRODUCTION

Every engineer that has worked on designing an integrated circuit has to leverage an understanding of device physics. Understanding device physics is essential when optimizing a design for speed, power, etc. These characteristics affect the bottom line when considering an integrated circuit used in a particular application. In order for there to be an understanding of device physics, there must be a device model that is developed for a device of interest. The development of a device model often involves utilizing fundamental physical equations in a manner that is solvable by either analytical or numerical means.

This typically begins by simplifying fundamental physical equations, possibly spanning multiple domains, and considering the physical quantities of interest. In order to make simplifications, assumptions about the underlying physics must be made. It is the process of transitioning from known physics laws to simplified mathematical models that a device modeler spans.

This thesis will cover the device modeling aspects of a new classification of computing devices, spintronics. It will begin by stating the physical assumptions necessary for the operation of spintronic devices. Then it will go the process of deriving the underlying physical equations and stating them in a tractable form with the appropriate boundary conditions. Then these equations will be manipulated and mapped into an equivalent circuit. The equivalent circuits will them be validated against analytical solutions provided from other works. It will then finish by providing example devices that can be simulated with the develop device models, and some optimization results are proposed based off a simplified circuit model.

1.1 Motivation

Spintronic devices utilize the properties of an electron's spin as a novel state variable for information storage, manipulation, and communication. Recent interest in spintronic devices is due to their potential as a low-power, CMOS process compatible computing devices [3, 4]. In order to leverage spintronic devices in circuit designs, compact circuit models of spin physics will be essential. Developing compact circuit models will require an understanding of the underlying physics governing spintronic devices.

In the case of spintronic devices, the underlying physics are well understood. The key interaction between spins in a spintronic device involves storing spin in a ferromagnetic body, and then transferring the angular momentum through a non-magnetic conductor into another ferromagnet. The physical behavior and resulting circuit theory of spintronic devices is detailed in [5, 6, 7, 8, 9, 4, 10, 11]. The physics governing the magnetization of the ferromagnetic body are predicted by the LLG equation [12, 13]. The transport properties of spin in a non-magnetic conductor are governed by the spin drift-diffusion equation [14, 15]. The mathematical relationship between the spin voltages and currents defined in [6], connects the physical quantities of spin storage in the ferromagnet to spin transport in the non-magnetic conductor. When coupled together, these equations form the basis for the simulation of spintronic devices.

Simulations of spintronic devices have been performed in [16, 3, 17]. In [16], a complete analysis of a ferromagnetic/non-magnetic stacked structure is performed *ab-initio* using quantum mechanical methods. While this model simulates all of the dynamics previously mentioned, it does not enable the development of a compact model suitable for circuit simulation. Ref. [3] solves the LLG equation and the steady-state spin transport equations by coupling the initial and boundary conditions of the relevant differential equations. This is accomplished by solving the magnetization dynamics in the time domain for one time step, Δt, then passing the solution as a boundary condition to the spin transport equations. This approach ignores the transient characteristics involved in the spin transport

physics. In [17], a compact circuit model simulates the LLG equation in ferromagnets, but this model only simulates a single type of spintronic device, the Magnetic Tunnel Junction (MTJ). The MTJ is formed by stacking an insulating material with ferromagnetic elements. In the interest of designing a broader class of spintronic devices, we would like to be able to simulate spin transport in a non-magnetic channel, something this model does not simulate.

1.2 Goals

In the process of developing compact, circuit simulation compatible models, we will seek to link the magnetization dynamics to the spin transport physics using the results obtained in [18]. In [18] the magnetization, $\vec{m}$, is linked to the spin transport quantities, $\overline{I}_s$ and $\overline{V}_s$ through a matrix-vector product. The main contribution of this work will be compact circuit models that are developed by mapping the equations governing the magnetization dynamics(the LLG equation), the spin transport physics (the spin drift-diffusion equation), and the connection between the two, spin injection, to equivalent circuits.

In this work, we seek to create a unified cohesive device and circuit simulation environment using basic electrical circuit elements such as resistors, capacitors, and current sources. This approach enables an easy construction and simulation of an equivalent circuit model for spintronic devices using a circuit solver such as HSPICE [19]. The circuit simulator can solve all underlying physical equations simultaneously with no need for going back and forth between numerical solvers. The circuit elements also provide intuition and insight into the operation of these emerging devices.

CHAPTER 2

DEVICE PHYSICS

2.1 Introduction

This work will seek to model the physics involved in the operation of spintronic devices in the hopes of developing compact circuit models suitable for circuit simulation.

2.2 Single-Domain Ferromagnets

We will begin by bridging the gap between the principles of macroscopic ferromagnetism commonly found in magnetic devices found in transformers, inductors, etc. These devices rely on Maxwell's equations to explain their operation. Spintronic devices, on the other hand, utilize single domain structures that require different physics developed in [1].

2.2.1 Magnetic Domains

Magnetic domains were postulated as a way to explain the hysteretic characteristics of a magnetized material. Weiss postulated that a "molecular" field is present that balances the thermal motion of particules. This field is justified by the quantum-mechanical exchange forces present in ferromagnetic materials and it explains the magnetization curves of ferromagnetic materials.

Domains structures balance the total energy of a sample by subdividing the magnetization vectors into different orientations until the energy required for subdivision is greater than the energy of the current configuration. This is shown in Fig. 1.

2.2.2 Single Domains

Spintronic devices utilize ferromagnet elements that are composed of only a single domain. Single domain ferromagnets exist when the dimensions of the sample are sufficiently small such that domain formation is impossible due to the fact the total energy of the sample is minimized as a single domain permanent magnet. In general, these dimensions occur when

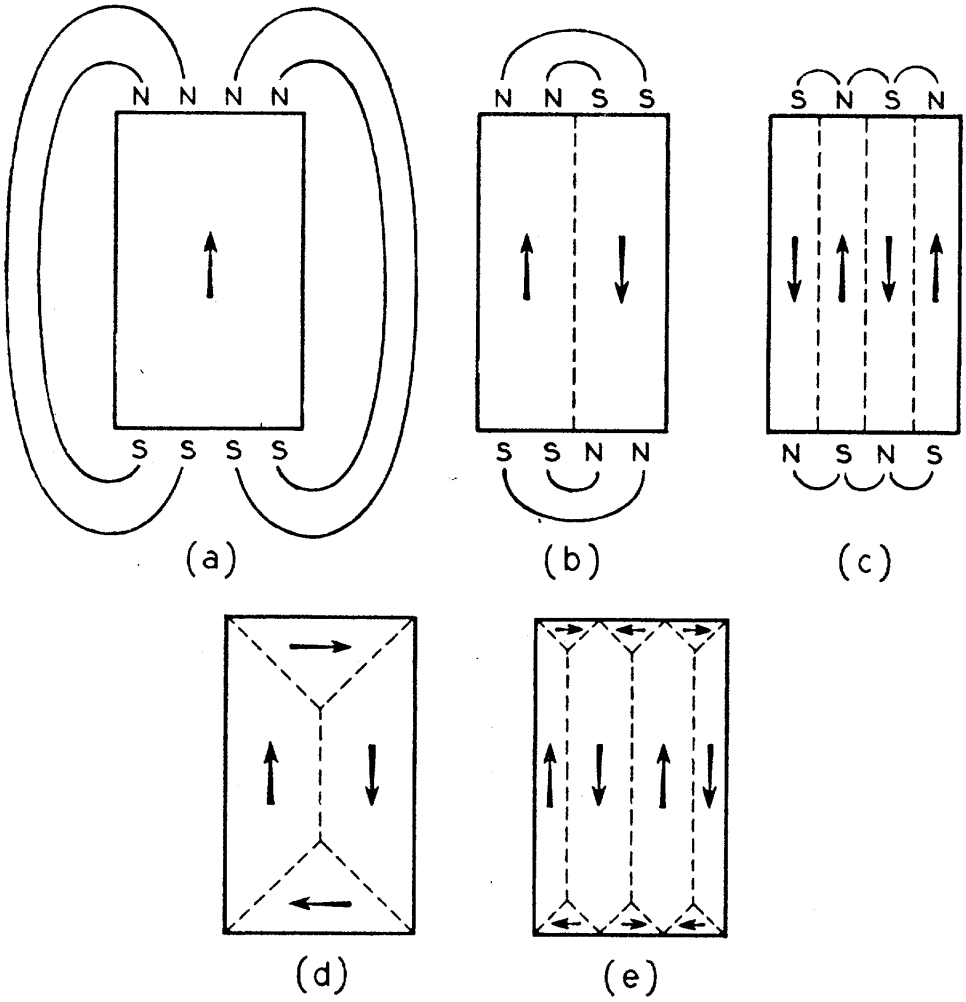

Figure 1: Division of Magnetic Domains (Image Source: [1]).

the Barkhausen effect [20] becomes negligible. In Fe, Ni, and Co this occurs around $10^{-}7$ m.

2.3 Stoner Particle Physics

Our first step in developing a compact circuit model for spintronic devices begins with developing an understanding of how the magnetization of single domain ferromagnets behaves over time. Landau and Lifshitz [12] suggested that the change in magnetization per unit time should be proportional to a torque applied to the normalized magnetization,

$\vec{m} = \frac{\vec{M}}{M_s}$,

$$\frac{d\vec{m}}{dt} \propto \vec{\tau}, \tag{1}$$

where τ is the total torque applied to the magnetization. The principles of this torque can be explained using the Stoner-Wohlfarth model [21]. This model states that the torque is comprised of the effect of the internal magnetic field, a torque due to damped motion, and the effect of spin transfer torque caused by spin current,

$$\vec{\tau} = \vec{\tau}_{\vec{H}} + \vec{\tau}_{\alpha} + \vec{\tau}_{\vec{I}_s}. \tag{2}$$

2.3.1 Magnetic Field Torque

The torque due to a magnetic field on a Stoner particle is generated since, in general, a magnetic dipole submerged in a magnetic field, $\vec{H}$, experiences a torque of,

$$\vec{\tau}_{\vec{H}} = \mu_0 \left(\vec{m} \times \vec{H}\right), \tag{3}$$

where the dipole has a magnetization of, $\vec{m}$, and μ_0 is the free space permeability. In order to compute the torque from the effective internal field, $\vec{\tau}_{\vec{H}}$, we need a constant of proportionality to factor in the torque correctly. We will use the gyromagnetic ratio, γ_0, which reflects the fact that a magnetization procession at steady state occurs at the Larmor frequency, $\omega_0 = \gamma_0 |H|$. This leaves us with the expression for the torque on a magnetic dipole due to a magnetic field,

$$\vec{\tau}_{\vec{H}} = \gamma_0 \mu_0 \left(\vec{m} \times \vec{H}\right). \tag{4}$$

The magnetic field, $\vec{H}$, for a single-domain, Stoner particle is explained in the Stoner-Wohlfarth field theory. It begins by considering the potential energy generated by a magnetic dipole,

$$E = -\mu_0 \int_V \vec{H} \cdot d\vec{M}. \tag{5}$$

The energy E is the total potential energy of the system, in this case the ferromagnetic body. The total energy of a ferromagnet can be computed using the Heisenberg Hamiltonian, which represents a magnetic system in terms of the total quantum mechanical spin.

The Stoner-Wohlfarth theory approximates this Hamiltonian by treating the entire ferromagnetic body as a macrospin, which is possible due to the assumptions stated in 2.2.

A macrospin results from weak anisotropy effects in magnetic nanoparticles of sufficient dimensions [1]. The entire magnetic body can be treated as a single spin with a magnetization proportional to the volume of the ferromagnet. The total potential energy accounts for the shape and composition of the ferromagnetic body. In the absence of an externally applied magnetic field, the energy of a Stoner particle is [22],

$$E = \frac{\mu_0 M_s^2 V}{2}\left(h_X \sin^2\theta\cos^2\phi + h_Y \sin^2\theta\sin^2\phi + h_Z\cos^2\theta\right), \tag{6}$$

where ϕ is the angle between the magnetization and the easy axis in the easy-plane, θ is the angle between the magnetization and the fixed layer, $\hat{z}$. The constants h_X, h_Y, and h_Z are determined by the shape and material of the ferromagnetic body. The energy of the macrospin depends on the Zeeman energy of the system, the magnetostatic energy, and the crystalline anisotropy energy of the system [23]. The Zeeman energy will be neglected for simplicity purposes in our circuit model. Zeeman energy is produced from an externally supplied magnetic field, and the devices that will be studied in this work do not utilize such fields for their operation. The magnetostatic energy is,

$$E_d = \frac{1}{2}\mu_0 V M_s \vec{m}\cdot\vec{H}_d, \tag{7}$$

where $\vec{H}_d$ is,

$$\vec{H}_d = M_s \overline{N}_d \vec{m}. \tag{8}$$

The quantity $\overline{N}_d$ is known as the demagnetization tensor with diagonal factors of N_x, N_y, and N_z, and can be computed according to the formulas presented in [24]. The crystalline anisotropy energy of the system is,

$$E_K = K_u V \sin^2\phi - \theta, \tag{9}$$

where K_u is the energy density of the particle and has been calculated for several materials using experimental data [22]. Combining the effects of the magnetostatic energy and the

crystalline anisotropy energy results in the following values for the constants h_X, h_Y, and h_Z,

$$\begin{aligned} h_X &= N_x - \frac{4K_u}{\mu_0 M_s^2 L_x} \\ h_Y &= N_y \\ h_Z &= N_z - \frac{H_k}{M_s} \end{aligned} \tag{10}$$

where H_k is the Stoner-Wholfarth field and L_x is the thickness of the ferromagnet perpendicular to the easy axis.

Using Eq. 5 the magnetic field can be calculated as,

$$\vec{H} = -\frac{1}{\mu_0 V}\frac{dE}{d\vec{M}}, \tag{11}$$

where we have taken advantage of the fact that the integral is calculated over the total volume of the ferromagnet. The magnetic field of a Stoner particle is therefore,

$$\begin{aligned} H_x &= -M_s h_X m_x \\ H_y &= -M_s h_Y m_y \\ H_z &= -M_s h_Z m_z \end{aligned} \tag{12}$$

The circuit model that will be developed later must also include a correction to the magnetic field in order to properly capture the effect of thermal noise on the ferromagnetic body. This will come in the form of a thermal field, $\vec{H}_T$,

$$\vec{H} = -\frac{1}{\mu_0 V}\frac{dE}{d\vec{M}} + \vec{H}_T, \tag{13}$$

The thermal field is due to the thermal motion of electrons and is statistical in nature. The joint distribution of the thermal field according to the theory developed by [25] is Gaussian with mean,

$$\langle \vec{H}_{T,i}(t) \rangle = 0. \tag{14}$$

The correlation between the components of $\vec{H}_T$ is defined over time interval τ as,

$$\langle \vec{H}_{T,i}(t)\vec{H}_{T,j}(t+\tau)\rangle = \frac{2k_bT\alpha}{\gamma V\mu_0 M_s}\delta_{ij}\delta(\tau). \tag{15}$$

The statistical properties of the thermal noise present in the ferromagnet will play an important role in the SPICE implementation of the circuit model. Most circuit simulators provide the capability of specifying Gaussian noise sources with a mean, Eq. 14, and magnitude, Eq. 15.

2.3.2 Damping Torque

The second torque term, τ_α is due to the presence of a damped motion proposed by Gilbert [13]. This torque exists since the magnetization exhibits a damped response towards equilibrium solutions. This creates the need for an additional torque term in our magnetization equation (Eq. 2). Gilbert added this term to the original equation proposed by Landau & Lifshitz,

$$\vec{\tau}_\alpha = \frac{\alpha}{M_s}\left(\vec{M}\times\frac{d\vec{M}}{dt}\right). \tag{16}$$

The torque term describes the damped oscillations in term of the cross product between the magnetization $\vec{M}$ and its temporal derivative, $\frac{d\vec{M}}{dt}$. The magnitude of the oscillations is controlled by the parameter α. The parameter α is a phenomenological parameter that can be calculated ab-initio from the quantum mechanical spin observable with spin-orbit coupling for different ferromagnetic materials [26].

2.3.3 Spin-Transfer Torque

The final term in the torque equation arises from the presence of spin-transfer torque in a system consisting of ferromagnets with non-collinear states, $\vec{m}_1 \neq \pm\vec{m}_2$. Such systems require the electron, as well as spin, current to flow from ferromagnet to ferromagnet. As a result, angular momentum is transferred between ferromagnets that contain transverse (perpendicular) components. Zangwill and co. [27] found that this absorbtion process is contributed to by the spin reflection and transmission coefficients at a material interface,

the rotation of the transmitted spins, and the spatial evolution of spins in the ferromagnet. Their formalism fully captures the quantum mechanical aspects of the material interface.

We take advantage of the fact that the torque equation approximates the entire ferromagnet as a single spin. The torque equation is normalized, so we will need to divide the total perpendicular spin current at the interface by the number of spins in the ferromagnet, N_s,

$$N_s = \frac{2M_sV}{\gamma_0\hbar}. \tag{17}$$

The torque generated will be proportional to the transverse component of the spin current at the interface. This magnitude will depend on the projection of the spin current to the magnetization. The general vector cross product that accounts for this projection is,

$$\vec{I}_{s,\perp} = \vec{m} \times \left(\vec{I}_s \times \vec{m}\right). \tag{18}$$

Therefore, the total torque due to the presence of spin-transfer torque is,

$$\vec{\tau}_s = \frac{\vec{m} \times \left(\vec{I}_s \times \vec{m}\right)}{qN_s}, \tag{19}$$

where we have used the unit charge, q, to normalize the torque term.

2.4 LLG Equation w/ Spin-Transfer Torque

By combining Eqs. 3-19 and substituting into Eq. 2, we can write the full LLG equation including the effect of spin-transfer torque,

$$\frac{d\vec{m}}{dt} = -\gamma\mu_0\left(\vec{m} \times \left(\vec{H} + \vec{H}_T\right)\right) + \alpha\left(\vec{m} \times \frac{d\vec{m}}{dt}\right) + \frac{\vec{I}_{s,\perp}}{qN_s}. \tag{20}$$

This equation will represent the magnetization dynamics of the ferromagnets present in the systems that we are interested in modeling. Our circuit models will therefore seek to mimic the dynamics of this equation.

2.5 Collinear & Non-collinear Magnetoelectronics

The 2-channel resistor model, 2, predicts the steady-state behavior of ferromagnetic devices with collinear magnetizations, $\vec{m}_1 \neq \pm\vec{m}_2$. This leads to phenomena such the Giant

Magnetoresistance (GMR) which is already well understood in other devices with ferromagnetic elements, such as the Magnetic Tunnel Junction (MTJ). The model splits the spin dependent quantities into spin up, ↑, and spin down, ↓ polarizations, essentially identical to the majority and minority carrier concentrations present in semiconductor transport. Separate branch currents are used in the circuit for spin up current, $I_\uparrow$, and spin down current, $I_\downarrow$. This results in separate conductances, $G_\uparrow$ and $G_\downarrow$ that represent the conductance of majority and minority spins as shown in Fig. 2. In this model the total electrical conductance is equal to $G = G_\uparrow + G_\downarrow$, and the total electrical current is equal to $I = I_\uparrow + I_\downarrow$. The spin quantities are represented by the spin conductance, $G_s = G_\uparrow - G_\downarrow$, the spin current, $I_s = I_\uparrow - I_\downarrow$, and the spin voltage, $V_s = \frac{1}{G_s} I_s$. Nodal analysis of the 2-channel model results in,

$$I_C = I_\uparrow + I_\downarrow = G_\uparrow \left(V_{C,N} + V_s - V_{C,F}\right) + G_\downarrow \left(V_{C,N} - V_s - V_{C,F}\right), \tag{21}$$

and

$$I_{s,\parallel} = I_\uparrow - I_\downarrow = G_\uparrow (V_{C,N} + V_s - V_{C,F}) - G_\downarrow (V_{C,N} - V_s - V_{C,F}), \tag{22}$$

where $I_{s,\parallel}$ is the spin current between collinear ferromagnets, $V_{C,N}$ is the charge voltage on the non-magnetic conductor side, and $V_{C,F}$ is the charge voltage on the ferromagnet side.

Understanding the interaction between non-collinear ferromagnets requires the same formalism that is used to prove the absorbtion of transverse spin currents. Additionally, we must extend our definition of the spin accumulation to include the vector spin voltages and spin currents in Cartesian coordinates,

$$\begin{aligned} \overline{V}_s(x,t) &= \begin{bmatrix} V_C & V_{s,x} & V_{s,y} & V_{s,z} \end{bmatrix}^T, \\ \overline{I}_s(x,t) &= \begin{bmatrix} I_C & I_{s,x} & I_{s,y} & I_{s,z} \end{bmatrix}^T. \end{aligned} \tag{23}$$

This is necessary for modeling the vectorial nature of the transverse spin quantities.

The transmission and reflection coefficients of the transverse electrons, $r_\uparrow^{nm}$ and $r_\downarrow^{nm}$ [16], capture the process of spin-flip at the ferromagnet/non-magnet (FM/NM) interface and are factored into the calculation of the perpendicular spin current,

$$\vec{I}_{s,\perp} = 2\mathrm{Re}G_{\uparrow\downarrow}\vec{m} \times \left(\vec{V}_s \times \vec{m}\right) + 2\mathrm{Im}G_{\uparrow\downarrow}\vec{V}_s \times \vec{m}. \tag{24}$$

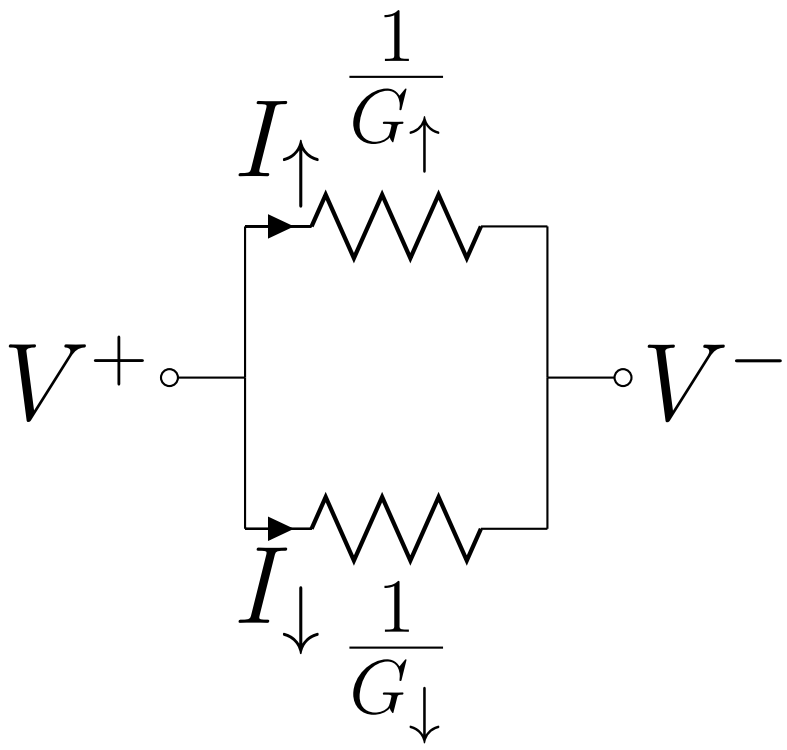

Figure 2: Two-Channel Resistor Model.

where $\vec{V}_s$ is the vector spin voltage that contains the Cartesian V_x, V_y, and V_z components, and the spin mixing conductance is calculated as,

$$G_{\uparrow\downarrow} = \frac{q^2}{h}\left(M - \sum_{nm} r_\uparrow^{nm}\left(r_\downarrow^{nm}\right)^*\right). \tag{25}$$

2.6 Ferromagnet to Non-magnetic Conductor Interface

An expression now needs to be derived to express the spin current at the interface as a function of a spin current of arbitrary direction specified in Cartesian Coordinates. We will begin by considering a magnetization that is aligned with the x-axis ($\vec{m} = \hat{x}$). The parallel spin current $\vec{I}_{s,\parallel}$ is then,

$$\vec{I}_{s,\parallel} = \vec{I}_{s,x} = \left(G_\uparrow\left(V_{C,N} + \vec{V}_{s,x} - V_{C,F}\right) - G_\downarrow\left(V_{C,N} - \vec{V}_{s,x} - V_{C,F}\right)\right)\hat{x}. \tag{26}$$

If the two transverse components of 18 are established as the orthogonal y and z axis then the resulting expression is,

$$\begin{aligned}
\vec{I}_{s,\perp} &= \vec{I}_{s,y} + \vec{I}_{s,z} \\
\vec{I}_{s,y} &= 2\mathrm{Re}G_{\uparrow\downarrow}V_{s,y}\hat{y} + 2\mathrm{Im}G_{\uparrow\downarrow}V_{s,z}\hat{y}, \\
\vec{I}_{s,z} &= 2\mathrm{Re}G_{\uparrow\downarrow}V_{s,z}\hat{z} - 2\mathrm{Im}G_{\uparrow\downarrow}V_{s,y}\hat{z}.
\end{aligned} \tag{27}$$

The formula for the change current also follows the two channel current model,

$$I_C = G_\uparrow(V_{C,N} + \vec{V}_{s,x} - V_{C,F}). \tag{28}$$

Equations 26 - 28 can be rewritten to express the tensor spin current as a function of the tensor spin voltage in the collinear case of $\vec{m} = \hat{x}$,

$$\begin{aligned}
\overline{I}_{S,\vec{m}=\hat{x}} &= \mathbf{G}_{\hat{x}}\overline{V}_{S,\vec{m}=\hat{x}} \\
\begin{bmatrix} I_C \\ I_{s,x} \\ I_{s,y} \\ I_{s,z} \end{bmatrix} &= \begin{bmatrix} G_\uparrow & G_\downarrow & 0 & 0 \\ G_\downarrow & G_\uparrow & 0 & 0 \\ 0 & 0 & 2\mathrm{Re}G_{\uparrow\downarrow} & 2\mathrm{Im}G_{\uparrow\downarrow} \\ 0 & 0 & -2\mathrm{Im}G_{\uparrow\downarrow} & 2\mathrm{Re}G_{\uparrow\downarrow} \end{bmatrix} \begin{bmatrix} V_{C,N} - V_{C,F} \\ V_{s,x} \\ V_{s,y} \\ V_{s,z} \end{bmatrix}.
\end{aligned} \tag{29}$$

This equation forms the basis for the derivation of the general non-collinear case. Modification of the spin conductance matrix, $\mathbf{G}_{\hat{x}}$ to include the polarization of the ferromagnetic element will enable the co-simulation of magnetization dynamics with spin transport using circuit simulation.

First, a 4×4 mathematical operator $\mathbf{R}_{\hat{x}}$ is defined to project the non-collinear circuit tensor quantities onto the collinear case, $\vec{m} = \hat{x}$,

$$\begin{aligned}
\overline{I}_{S,\vec{m}=\hat{x}} &= \mathbf{R}_{\hat{x}}\overline{I}_S \\
\overline{V}_{S,\vec{m}=\hat{x}} &= \mathbf{R}_{\hat{x}}\overline{V}_S.
\end{aligned} \tag{30}$$

We now solve Eq. 30 for $\overline{I}_S$ and $\overline{V}_S$,

$$\begin{aligned}
\overline{I}_S &= \mathbf{R}_{\hat{x}}^{-1}\overline{I}_{S,\vec{m}=\hat{x}} \\
\overline{I}_{S,\vec{m}=\hat{x}} &= \mathbf{G}_{\hat{x}}\mathbf{R}_{\hat{x}}\overline{V}_S \\
\overline{I}_S &= \mathbf{R}_{\hat{x}}^{-1}\mathbf{G}_{\hat{x}}\mathbf{R}_{\hat{x}}\overline{V}_S \\
\overline{I}_S &= \mathbf{G}_{\vec{m}}\overline{V}_S . \qquad (31)
\end{aligned}$$

where $\mathbf{G}_{\vec{m}}$ is the spin dependent conductance matrix for the general non-collinear case, and this final equation is what is referred to as Spin Ohm's Law [28].

2.7 Spin Particle Transport in Non-magnetic Conductors

A spin polarized current will undergo a change in magnitude as it flows through a non-magnetic conductor. This loss in spin current is due to a physical mechanism called spin relaxation. The spin transport model considered here is based on the macroscopic limit of the Valet & Fert theory developed in [14].

By considering the flow of majority and minority spin carriers, a drift-diffusion description of spin transport can be developed that closely resembles the description of charge flow in semiconductors. This begins by considering the random-walk motion of majority and minority spins [29]. If majority spins have a density of $n_\uparrow$ and minority spins have a density of $n_\downarrow$, then the overall spin density, s, is $s = n_\uparrow - n_\downarrow$. If we assume that the overall probability of spin flipping during a time interval, τ (spins switching from majority to minority or vice versa), ω, is less than 1, then we can write a taylor expansion for the majority and minority spin densities,

$$\begin{aligned}
\frac{\partial n_\uparrow}{\partial t} &= D\frac{\partial^2 n_\uparrow}{\partial x^2} - v_d\frac{\partial n_\uparrow}{\partial x} - \omega\left(n_\uparrow - n_\downarrow\right) \\
\frac{\partial n_\downarrow}{\partial t} &= D\frac{\partial^2 n_\downarrow}{\partial x^2} - v_d\frac{\partial n_\downarrow}{\partial x} - \omega\left(n_\downarrow - n_\uparrow\right). \qquad (32)
\end{aligned}$$

This results in the drift-diffusion equation for the overall spin density,

$$\frac{\partial s}{\partial t} = D\frac{\partial^2 s}{\partial x^2} - v_d\frac{\partial s}{\partial x} - \frac{s}{\tau_s}, \qquad (33)$$

where,

$$\tau_s = \frac{\tau}{2\omega}, \tag{34}$$

and,

$$v_d = -\mu E. \tag{35}$$

The evolution of the spin drift-diffusion equation depends on the length of the conductor, L_{int}, the electron mobility, μ, the diffusion coefficient, D, the spin relaxation time, τ_s, and, in the case of semiconductors, the electric field intensity, E. In [30] the electron mobility, the diffusion coefficient, and the spin relaxation time are calculated for different nano-scale materials as a function of the channel width, height, aspect ratio, specularity, and reflectivity. Process technology will limit all of these except the width, so we will look at the effect of varying width on these parameters. Figure 3 shows μ, D, and τ_s as a function of the conductor width for copper conductors. These results illustrate that a larger width contributes to higher diffusivity, mobility, and a longer spin relaxation time.

Equation 33 can be written as a continuity equation that expresses the change in spin density as a function of the current concentration,

$$\frac{\partial s}{\partial t} + \frac{\partial}{\partial x}\left(-\mu E s - D\frac{\partial s}{\partial x}\right) = -\frac{s}{\tau_s}, \tag{36}$$

where the section in parenthesis is recognized as the spin particle current density,

$$J_s = -\mu E s - D\frac{\partial s}{\partial x}. \tag{37}$$

This partial differential differential equation does not contain any analytical solutions for the drift-diffusion case. Analytical solutions can be derived for the diffusion only case with appropriate boundary conditions, and we will later use this to validate the spatial discretization that approximates the spatial derivative, ∂x, present in the equation. An important question to ask at this point concerns the average length a spin diffuses until it flips. This length is known as the spin diffusion length,

$$L_s = \sqrt{D\tau_s}. \tag{38}$$

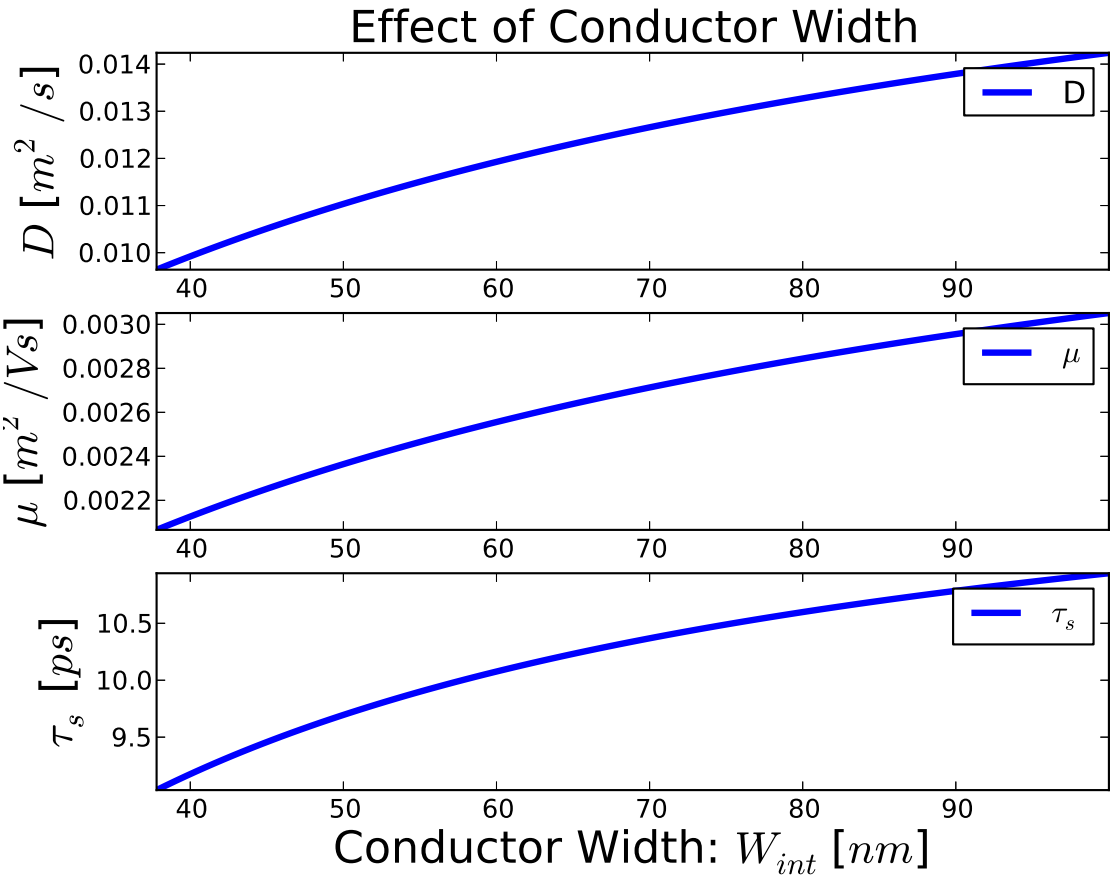

Figure 3: Spin Transport Parameters vs. Conductor Width.

This spin diffusion length approximates the average length that a spin polarized carrier travels before flipping polarities. Metals, while having a higher conductivity, often have shorter spin diffusion lengths. Figure 4 shows the spin diffusion length as a function of the conductor width. Longer spin diffusion lengths are often desirable in spintronic circuits since it it is analogous to longer minority carrier diffusion lengths in semiconductors. This leads to a smaller loss in spin current as it travels across conductors. We can also look at the influence of the conductor width on the spin diffusion length as shown in Fig. 4. Since larger widths results in smaller probabilities of electron collisions with with conductor boundaries, we see an improvement in L_s with larger widths.

This effect can be examined by solving Eq. 33 numerically and looking at the resulting

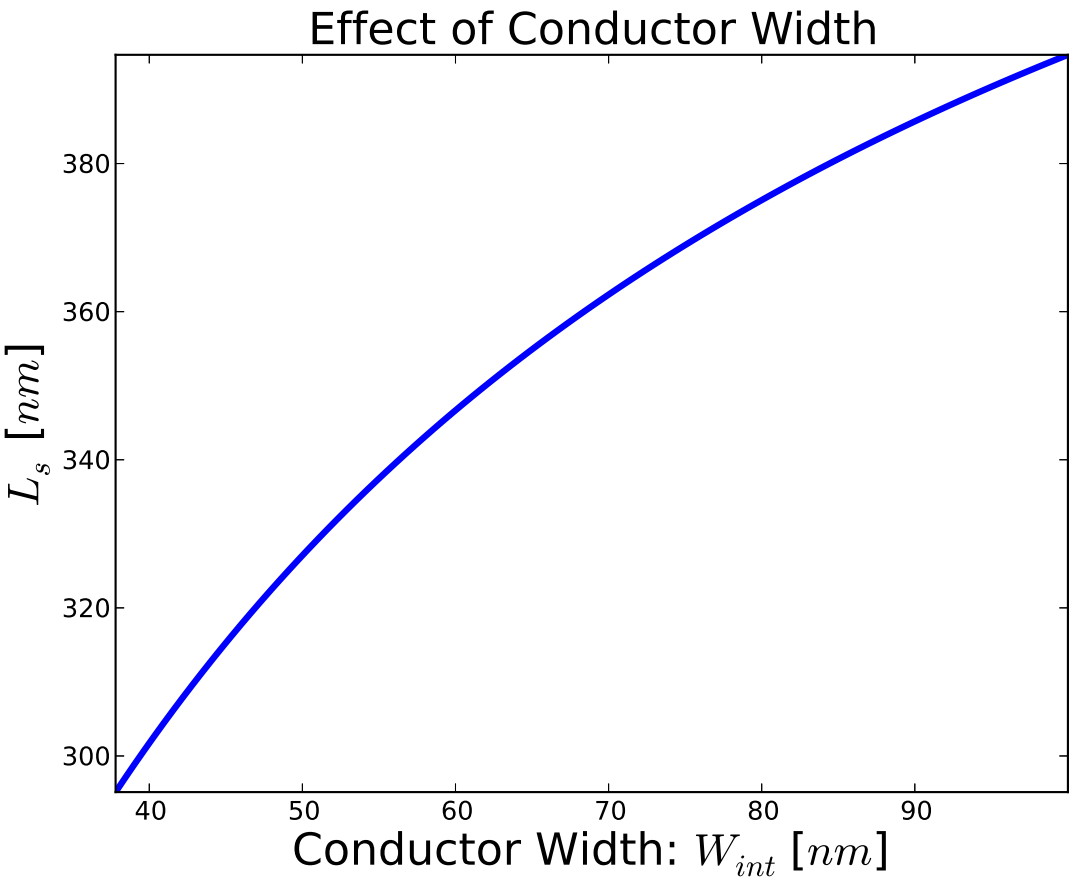

Figure 4: Spin Diffusion Length vs. Conductor Width.

spin current density, J_s. Figure 5 shows the spin current density entering a conductor, $J_{s,0}$, and the spin current density measured at the end of a conductor, $J_{s,L}$, for different spin diffusion lengths. As the spin diffusion length increases, we expect the magnitude of the spin current measured at the end of a conductor to be larger, since longer spin diffusion lengths result in fewer spins changing polarities. We also notice that longer spin diffusion lengths result in decreased delay as the input spin current, $J_{s,0}$, changes.

In addition to the width, we can also look at the effect that changing the conductor length, L_{int}, has on Eq. 33. We expect that the magnitude of the spin current also decreases for longer conductors. Figure 6 shows the numerical solution of Eq. 33 for multiple values of L_{int}. The steady-state part of the spin current density decreases for longer channel

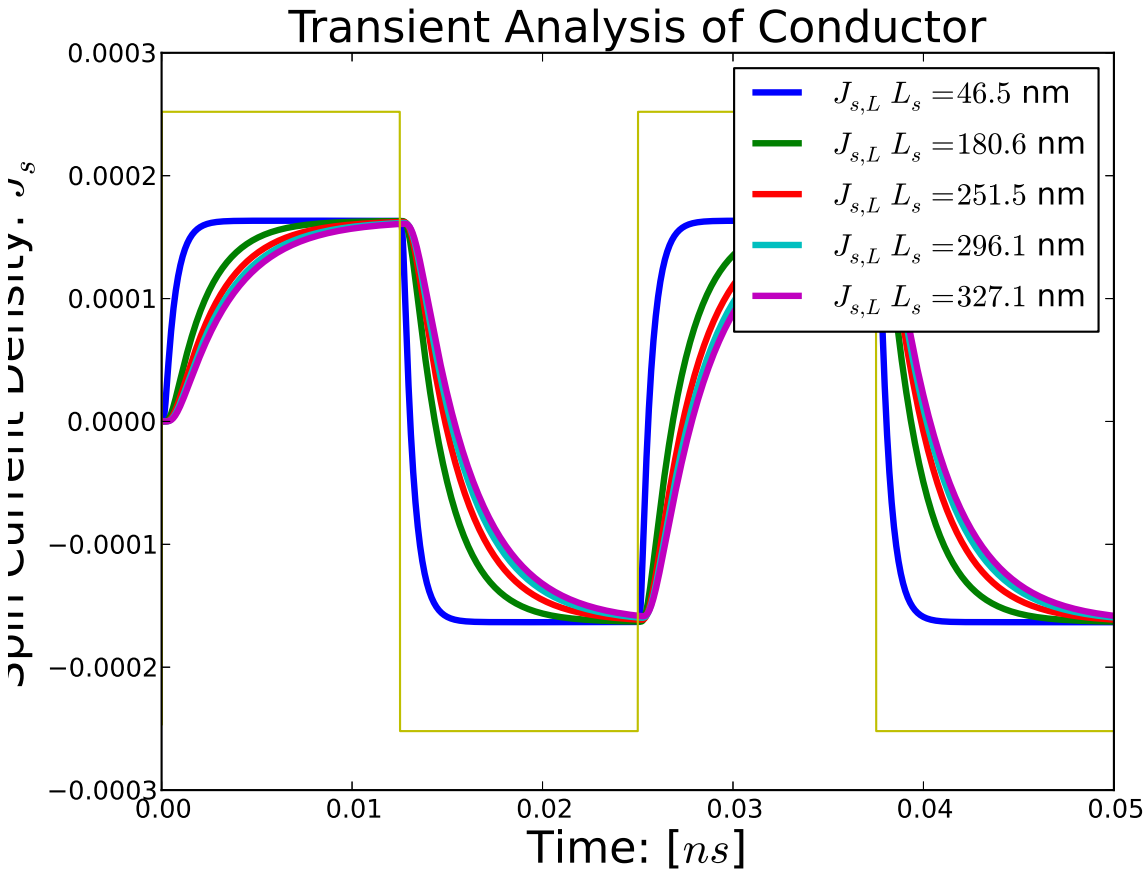

Figure 5: Spin Current Density for Multiple Spin Diffusion Lengths.

lengths. In a later section, we will quantify the change in steady state spin current density as a function of the channel length using an analytical solution presented in [29].

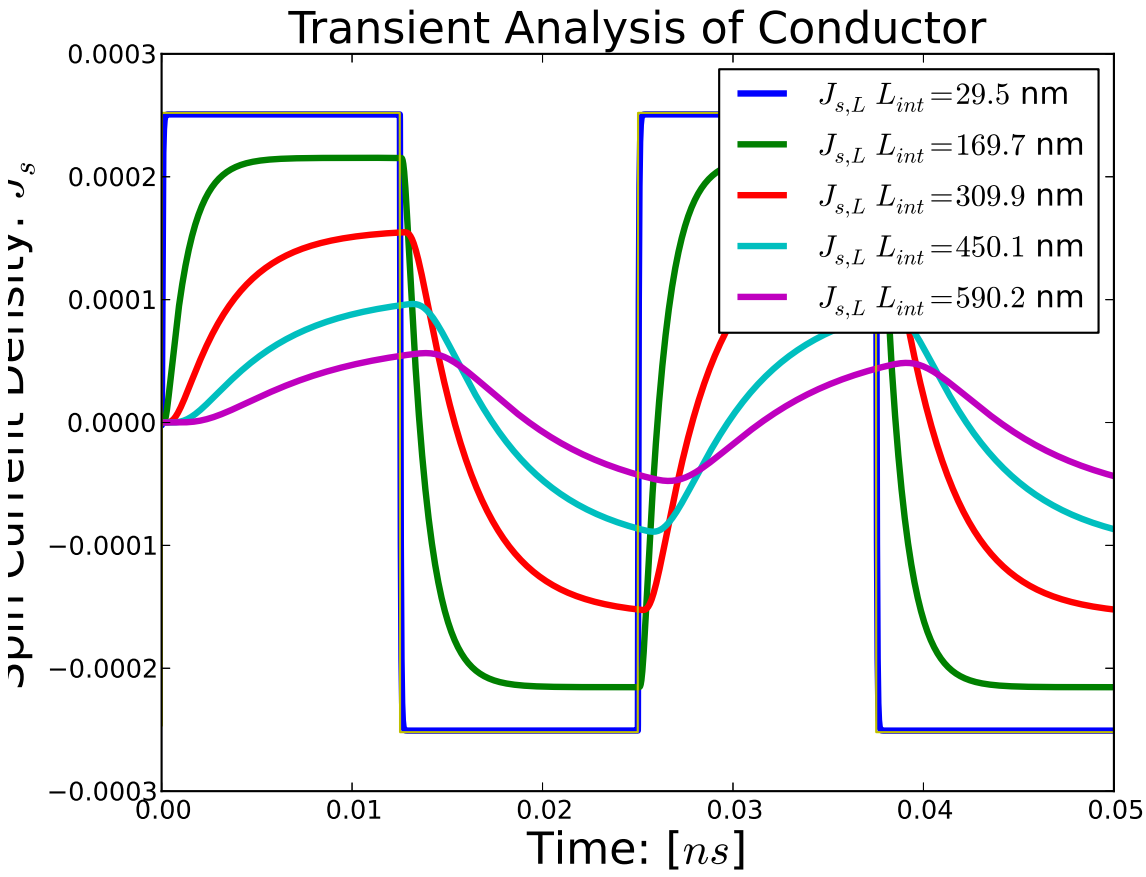

Figure 6: Spin Current Density for Multiple Conductor Lengths.

CHAPTER 3

CIRCUIT MODELS FOR SPIN STORAGE, INJECTION, AND TRANSPORT

The physical equations presented in the previous chapter will now be modeled using circuit components for use in circuit simulation. This will enable a complete simulation of spintronic devices using the SPICE circuit simulator. The circuit models will encompass the physics of spin storage, spin injection, and spin transport. In order to properly couple the magnetization dynamics with the spin transport equations, the circuit model will need to simulate the interdependence of the following variables according to the physical equations: $\overline{V}_s$, $\overline{I}_s$, and $\vec{m}$. This will be accomplished by modeling $\overline{V}_s$, $\vec{H}$, and $\vec{m}$ using node voltages, and by modeling $\overline{I}_s$ using branch currents.

3.1 Spin Storage

The development of an equivalent circuit for the magnetization dynamics requires refactoring the LLG equation, which is restated here

$$\frac{d\vec{m}}{dt} = -\gamma_0\mu_0\left(\vec{m}\times\vec{H}\right) + \alpha\left(\vec{m}\times\frac{d\vec{m}}{dt}\right) + \frac{\vec{m}\times\left(\vec{I}_s\times\vec{m}\right)}{qN_s}, \tag{39}$$

where we have divided by the saturation magnetization, M_s, in order to normalize the dependent variable, $\vec{m}$, and the effective magnetic field, $\vec{H} = H_k\vec{h}$. Equation 39 can be written as a system of differential equations in terms of $\frac{d\vec{m}}{dt}$ by taking the cross products and

writing the resulting system,

$$\begin{aligned}
\frac{dm_x}{dt} &= \left(\frac{dm_z}{dt}m_y - \frac{dm_y}{dt}m_z\right)\alpha - \left(H_{\text{eff},z}m_y - H_{\text{eff},y}m_z\right)\gamma\mu \\
&\quad + \frac{-I_{S,y}m_xm_y + I_{S,x}m_y^2 - I_{S,z}m_xm_z + I_{S,x}m_z^2}{N_sq}, \\
\frac{dm_y}{dt} &= \left(-\frac{dm_z}{dt}m_x + \frac{dm_x}{dt}m_z\right)\alpha - \left(-H_{\text{eff},z}m_x + H_{\text{eff},x}m_z\right)\gamma\mu \\
&\quad + \frac{I_{S,y}m_x^2 - I_{S,x}m_xm_y - I_{S,z}m_ym_z + I_{S,y}m_z^2}{N_sq}, \\
\frac{dm_z}{dt} &= \left(\frac{dm_y}{dt}m_x - \frac{dm_x}{dt}m_y\right)\alpha - \left(H_{\text{eff},y}m_x - H_{\text{eff},x}m_y\right)\gamma\mu \\
&\quad + \frac{I_{S,z}m_x^2 + I_{S,z}m_y^2 - I_{S,x}m_xm_z - I_{S,y}m_ym_z}{N_sq}.
\end{aligned} \tag{40}$$

Equation 40 is a linear system in $\frac{d\vec{m}}{dt}$ and can be solved to write,

$$\begin{aligned}
\frac{dm_x}{dt} &= -\frac{1}{N_sq\,(1+\alpha^2)}(I_{S,y}m_xm_y - I_{S,x}m_y^2 + I_{S,z}m_xm_z - I_{S,x}m_z^2 - I_{S,z}m_x^2m_y\alpha \\
&\quad - I_{S,z}m_y^3\alpha + I_{S,y}m_x^2m_z\alpha + I_{S,y}m_y^2m_z\alpha - I_{S,z}m_ym_z^2\alpha + I_{S,y}m_z^3\alpha + H_{\text{eff},z}m_yN_sq\gamma\mu \\
&\quad - H_{\text{eff},y}m_zN_sq\gamma\mu_0 + H_{\text{eff},y}m_xm_yN_sq\alpha\gamma\mu_0 - H_{\text{eff},x}m_y^2N_sq\alpha\gamma\mu_0 \\
&\quad + H_{\text{eff},z}m_xm_zN_sq\alpha\gamma\mu_0 - H_{\text{eff},x}m_z^2N_sq\alpha\gamma\mu_0), \\
\frac{dm_y}{dt} &= -\frac{1}{N_sq\,(1+\alpha^2)}(-I_{S,y}m_x^2 + I_{S,x}m_xm_y + I_{S,z}m_ym_z - I_{S,y}m_z^2 + I_{S,z}m_x^3\alpha \\
&\quad + I_{S,z}m_xm_y^2\alpha - I_{S,x}m_x^2m_z\alpha - I_{S,x}m_y^2m_z\alpha + I_{S,z}m_xm_z^2\alpha - I_{S,x}m_z^3\alpha \\
&\quad - H_{\text{eff},z}m_xN_sq\gamma\mu_0 + H_{\text{eff},x}m_zN_sq\gamma\mu_0 - H_{\text{eff},y}m_x^2N_sq\alpha\gamma\mu_0 + H_{\text{eff},x}m_xm_yN_sq\alpha\gamma\mu_0 \\
&\quad + H_{\text{eff},z}m_ym_zN_sq\alpha\gamma\mu_0 - H_{\text{eff},y}m_z^2N_sq\alpha\gamma\mu_0), \\
\frac{dm_z}{dt} &= -\frac{1}{N_sq\,(1+\alpha^2)}(-I_{S,z}m_x^2 - I_{S,z}m_y^2 + I_{S,x}m_xm_z + I_{S,y}m_ym_z - I_{S,y}m_x^3\alpha \\
&\quad + I_{S,x}m_x^2m_y\alpha - I_{S,y}m_xm_y^2\alpha + I_{S,x}m_y^3\alpha - I_{S,y}m_xm_z^2\alpha + I_{S,x}m_ym_z^2\alpha \\
&\quad + H_{\text{eff},y}m_xN_sq\gamma\mu_0 - H_{\text{eff},x}m_yN_sq\gamma\mu_0 - H_{\text{eff},z}m_x^2N_sq\alpha\gamma\mu_0 - H_{\text{eff},z}m_y^2N_sq\alpha\gamma\mu_0 \\
&\quad + H_{\text{eff},x}m_xm_zN_sq\alpha\gamma\mu_0 + H_{\text{eff},y}m_ym_zN_sq\alpha\gamma\mu_0).
\end{aligned} \tag{41}$$

By rewriting Eq. 41 the LLG equation can be modeled using an equivalent circuit representation,

$$\begin{aligned}
\frac{dm_x}{dt} &= \frac{f\left(\vec{m}, \vec{I}_s, \vec{H}_{eff}\right)}{N_s q\left(1+\alpha^2\right)} \\
\frac{dm_y}{dt} &= \frac{g\left(\vec{m}, \vec{I}_s, \vec{H}_{eff}\right)}{N_s q\left(1+\alpha^2\right)} \\
\frac{dm_z}{dt} &= \frac{h\left(\vec{m}, \vec{I}_s, \vec{H}_{eff}\right)}{N_s q\left(1+\alpha^2\right)}
\end{aligned} \tag{42}$$

Since $\vec{m}$ is modeled using a node voltage, the temporal derivative of 42 can be simulated using a capacitance since the node voltage on a capacitor follows, $C\frac{dv_c}{dt} = i_c$, where

$$C = N_s q\left(1+\alpha^2\right), \tag{43}$$

and,

$$\begin{aligned}
i_c &= f\left(\vec{m}, \vec{I}_s, \vec{H}_{eff}\right) \\
i_c &= g\left(\vec{m}, \vec{I}_s, \vec{H}_{eff}\right) \\
i_c &= h\left(\vec{m}, \vec{I}_s, \vec{H}_{eff}\right),
\end{aligned} \tag{44}$$

This results in the equivalent circuit, Fig. 7, where we have used non-linear voltage dependent current sources to model the spin-transfer torque calculated using the right-hand side of Eq. 42. The effective magnetic field, $\vec{H}_{eff}$, is modeled using voltage dependent voltage sources.

3.1.1 Thermal Noise Validation

The presence of thermal noise affects the transient characteristics of the magnetization dynamics. Thermal noise is caused by the thermally agitated motion of electrons in the ferromagnet [31]. Thermal noise leads to the presence of a thermal field, $\vec{H}_T$, in 15. An

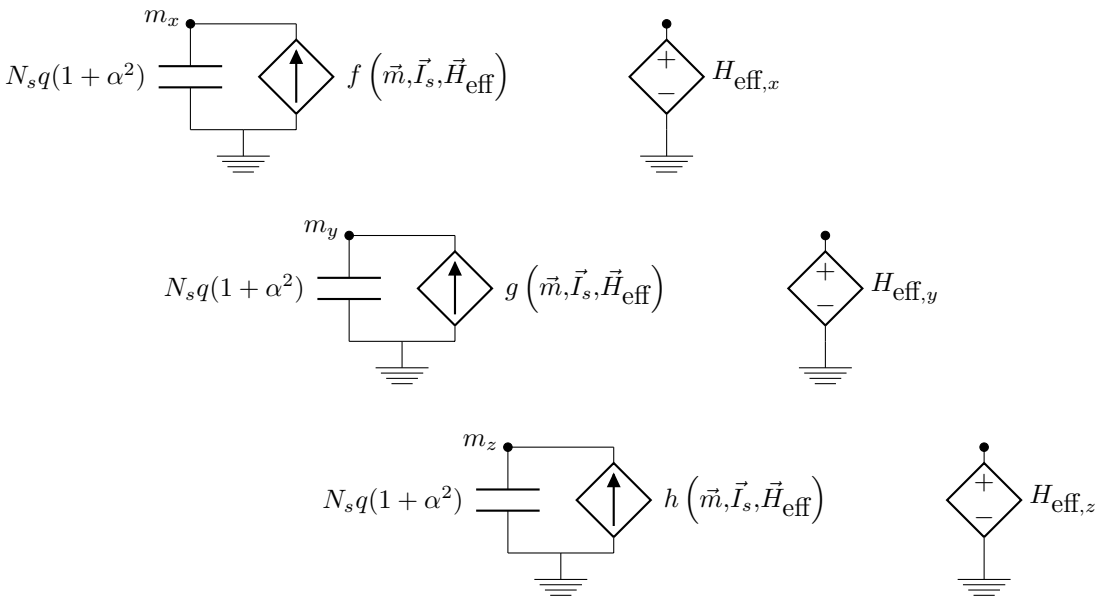

Figure 7: Circuit Model for the magnetization, $\vec{m}$.

analytical solution exists for the steady-state procession angle, θ_0, based off of the formulas presented by [31] as a function of the ferromagnet temperature,

$$\langle \theta_0^2 \rangle = \frac{k_b T}{E_b}. \tag{45}$$

In Fig. 8 the ferromagnet model is simulated under varying temperatures, and the steady-state angle measured from SPICE matches the analytical solution within 5%.

3.1.2 LLG Equation Validation

The behavior of the LLG equation must be duplicated by the ferromagnet circuit model. Analytical solutions of the LLG equation are difficult to obtain and do not accurately represent all of the physical cases that will be encountered during circuit simulation [23]. The differential equation solver, LSODA [32], has been used to obtain numerical solutions of the LLG equation. The numerical simulation has been performed with the initial conditions, $\vec{m}_i = \begin{bmatrix} m_x = 1 & m_y = 0 & m_z = 0 \end{bmatrix}^{\mathrm{T}}$, boundary conditions, $\vec{I}_s = \begin{bmatrix} I_{s,x} = 3mA & I_{s,y} = 0mA & I_{s,z} = 0m$ in the absence of thermal noise. In Fig. 9, the ferromagnet circuit model was simulated under identical conditions, and the results obtained from SPICE match identically with the

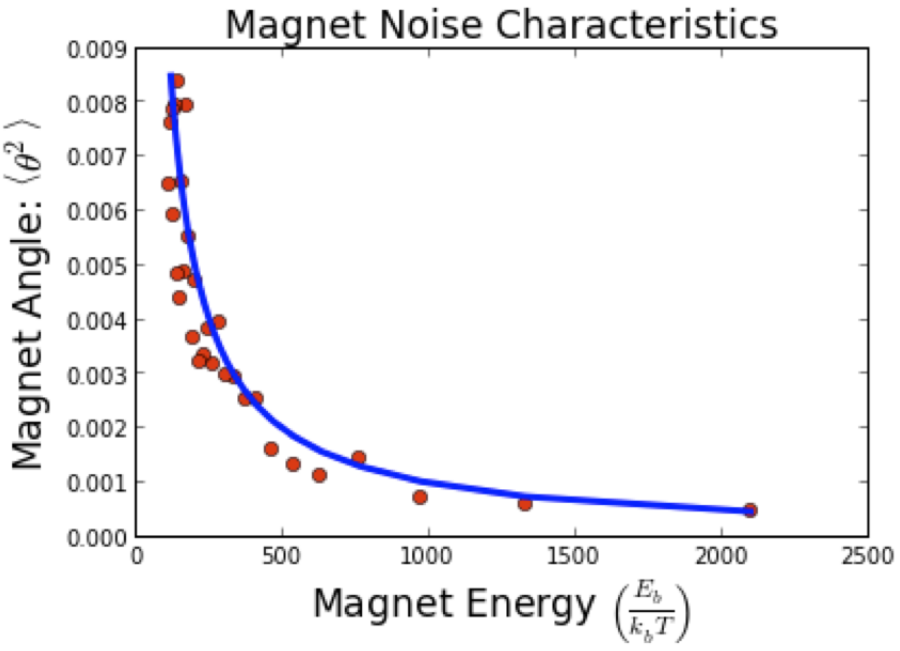

Figure 8: Ferromagnet Noise Analysis. Red symbols represent the circuit simulations while the blue curve shows the solution of 45.

results obtained from the LSODA simulation.

3.1.2.1 Ferromagnet Switching Time

The switching delay of a ferromagnet has been computed by [33] using the small cone-angle approximation. The delay, τ_{sw}, according to the small cone-angle approximation is,

$$\tau_{sw} = \frac{M_s V q}{I_{s,cr}\mu_b} \frac{\log \pi/\theta_0}{\chi - 1}. \tag{46}$$

We have used (83) as an additional method for validating the compact circuit model. The comparison with the SPICE simulations is shown in Fig. 10.

3.2 Spin Injection

The circuit model for spin injection computes the spin current across an interface as a function of the interface parameters and the polarization of the magnetization according to the magnetization dynamics. An expression for Spin Ohm's Law (Eq. 31) has already been

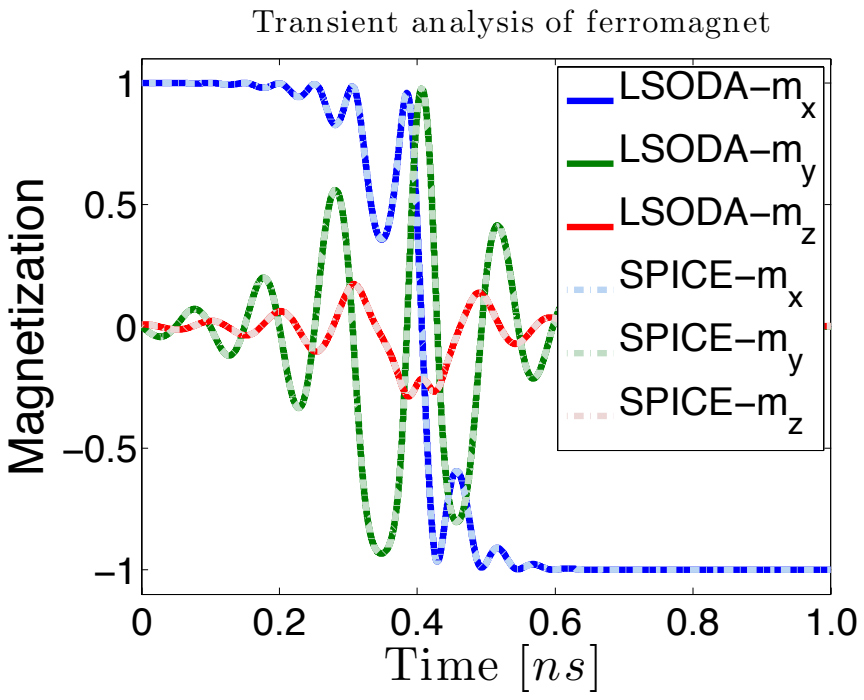

Figure 9: Ferromagnet Transient Analysis (w/o Thermal Noise).

presented,

$$\bar{I}_S = \mathbf{R}_{\hat{x}}^{-1}\mathbf{G}_{\hat{x}}\mathbf{R}_{\hat{x}}\bar{V}_S, \tag{47}$$

where the rotation operator, $\mathbf{R}_{\hat{x}}$, and it's matrix inverse need to be derived and then computed during simulation. The rotation operator can be derived by considering the effect of the magnetization on the current tensor, $\bar{I}_s$, and then projecting the perpendicular component of $\vec{I}_s$ onto the x-axis. Since the magnitude of the charge current should remain unchanged and decoupled from the spin current during the projection, we will define the rotation operator as follows,

$$\mathbf{R}_{\hat{x}} = \begin{bmatrix} 1 & 0 & 0 & 0 \\ 0 & r_{x,x} & r_{x,y} & r_{x,z} \\ 0 & r_{y,x} & r_{y,y} & r_{y,z} \\ 0 & r_{z,x} & r_{z,y} & r_{z,z} \end{bmatrix}, \tag{48}$$

where the first row and column leave the magnitude of I_C unchanged. The $r_{i,j}$ components project the ith component of a vector onto the jth component on the Cartesian Coordinate

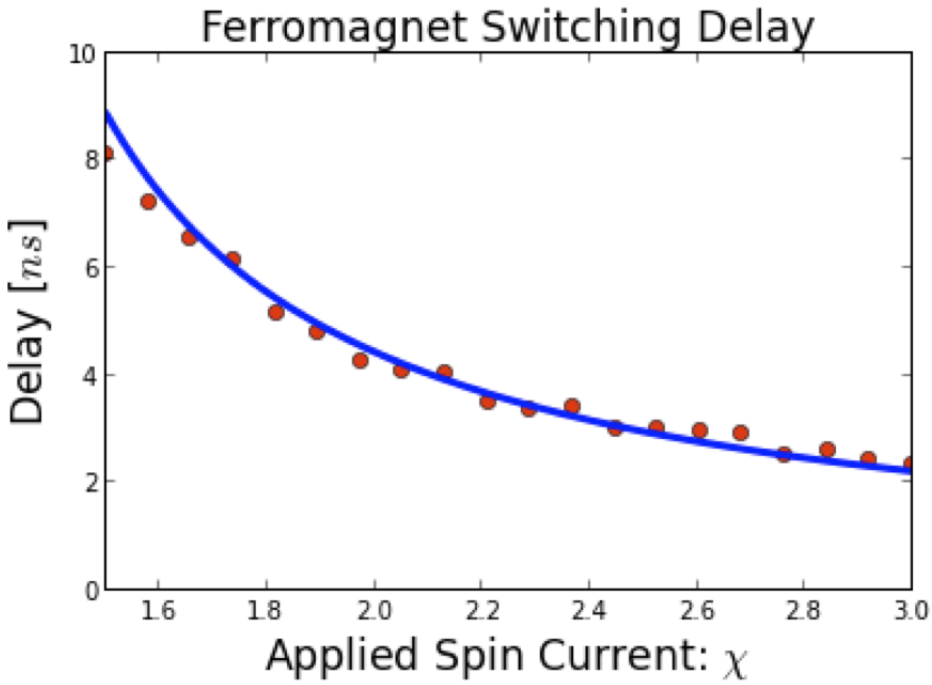

Figure 10: Ferromagnet Switching Delay. A spin current of $\chi I_{s,cr}$ is applied to the ferromagnet and the resulting switching delay is measured. Red symbols represent the circuit simulations while the blue curve shows the analytical solution.

Axis. The value for $\vec{r}_x$ is simply the projection of the spin current onto the unit vector $\hat{x}$,

$$\vec{r}_x = \vec{m} \tag{49}$$

The remaining vectors, $\vec{r}_y$ and $\vec{r}_z$, are simply the two transverse vectors that are perpendicular to both $\vec{m}$ and $\hat{x}$,

$$\begin{aligned} \vec{r}_y &= \hat{x} \times \vec{r}_x \\ \vec{r}_z &= \vec{r}_x \times \vec{r}_y. \end{aligned} \tag{50}$$

The multiplication of $\mathbf{R}_{\hat{x}}^{-1}\mathbf{G}_{\hat{x}}\mathbf{R}_{\hat{x}}$ in Eq. 47 can be carried out symbolically for use in a circuit model,

$$\mathbf{G}_{\vec{m}} = \mathbf{R}_{\hat{x}}^{-1}\mathbf{G}_{\hat{x}}\mathbf{R}_{\hat{x}} = \begin{bmatrix} g_{C,C} & g_{C,x} & g_{C,y} & g_{C,z} \\ g_{x,C} & g_{x,x} & g_{x,y} & g_{x,z} \\ g_{y,C} & g_{y,x} & g_{y,y} & g_{y,z} \\ g_{z,C} & g_{z,x} & g_{z,y} & g_{z,z} \end{bmatrix}, \tag{51}$$

where,

$$g_{C,C} = G_{\uparrow}, \tag{52}$$

$$g_{C,x} = G_{\downarrow} m_x, \tag{53}$$

$$g_{C,y} = G_{\downarrow} m_y, \tag{54}$$

$$g_{C,z} = G_{\downarrow} m_z, \tag{55}$$

$$g_{x,C} = G_{\downarrow} m_x, \tag{56}$$

$$g_{x,x} = G_{\uparrow} m_x^2 + \Re G_{\uparrow\downarrow} m_y^2 + \Re G_{\uparrow\downarrow} m_z^2, \tag{57}$$

$$g_{x,y} = -\left(\Re G_{\uparrow\downarrow} - G_{\uparrow}\right) m_x m_y + \Im G_{\uparrow\downarrow} m_z, \tag{58}$$

$$g_{x,z} = -\Im G_{\uparrow\downarrow} m_y - \left(\Re G_{\uparrow\downarrow} - G_{\uparrow}\right) m_x m_z, \tag{59}$$

$$g_{y,C} = G_{\downarrow} m_y, \tag{60}$$

$$g_{y,x} = -\left(\Re G_{\uparrow\downarrow} - G_{\uparrow}\right) m_x m_y - \Im G_{\uparrow\downarrow} m_z, \tag{61}$$

$$g_{y,y} = \Re G_{\uparrow\downarrow} m_x^2 + G_{\uparrow} m_y^2 + \Re G_{\uparrow\downarrow} m_z^2, \tag{62}$$

$$g_{y,z} = \Im G_{\uparrow\downarrow} m_x^3 - \left(\Re G_{\uparrow\downarrow} - G_{\uparrow}\right) m_y m_z + \Im G_{\uparrow\downarrow} m_x m_z + \frac{\Im G_{\uparrow\downarrow} m_x m_y^2 - \Im G_{\uparrow\downarrow} m_x^3 m_y^2}{m_y^2 + m_z^2}, \tag{63}$$

$$g_{z,C} = G_{\downarrow} m_z, \tag{64}$$

$$g_{z,x} = \Im G_{\uparrow\downarrow} m_y - \left(\Re G_{\uparrow\downarrow} - G_{\uparrow}\right) m_x m_z, \tag{65}$$

$$g_{z,y} = -\Im G_{\uparrow\downarrow} m_x \left(1 + m_y^2\right) - \left(\Re G_{\uparrow\downarrow} - G_{\uparrow}\right) m_y m_z + \frac{\Im G_{\uparrow\downarrow} m_x m_y^2 - \Im G_{\uparrow\downarrow} m_x^3 m_y^2}{m_y^2 + m_z^2}, \tag{66}$$

$$g_{z,z} = \Re G_{\uparrow\downarrow} \left(m_x^2 + m_y^2\right) + G_{\uparrow} m_z^2. \tag{67}$$

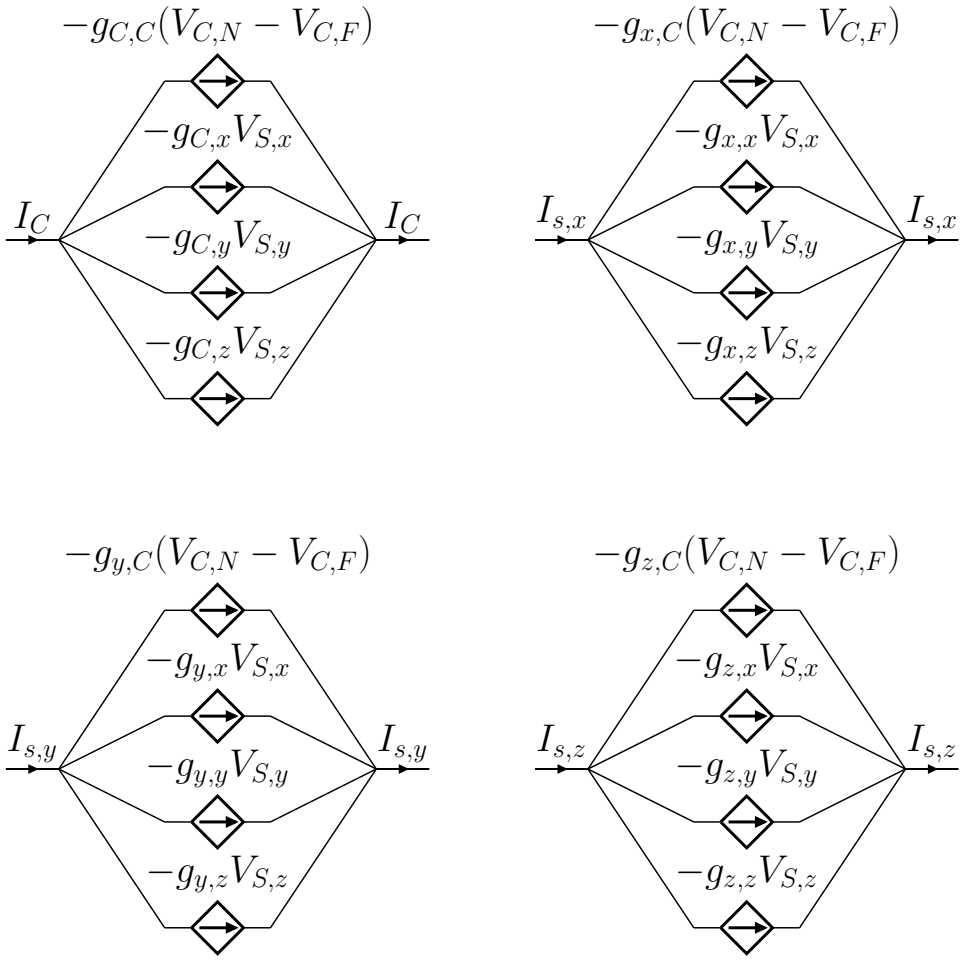

Figure 11: Interface Circuit Model.

This results in the equivalent circuit for spin injection, Fig. 11, where voltage dependent current sources have been used to model Spin Ohm's Law and simulate the tensor current through a ferromagnetic/non-magnetic conductor interface.

3.3 Development of a SPICE Equivalent Circuit Model for Spin Transport

The drift-diffusion equations model the transport of charge and spin in non-magnetic conductors. The charge diffusion equation is the continuity equation, where I_C is the current

due to diffusion current only,

$$\begin{aligned} C_e \frac{\partial V_C}{\partial t} &= \frac{\partial I_C}{\partial x} \\ I_C &= \sigma A \frac{\partial V_C}{\partial x}, \end{aligned} \tag{68}$$

where C_e is the electrostatic capacitance per unit length, σ is the conductivity of the non-magnetic conductor, and A is the cross-sectional area. This equation results in the familiar circuit model for an RC interconnect of an infinitesimal length shown in the upper-left corner of Fig. 12. The spin drift-diffusion equation is the continuity equation for the spin accumulation, $\vec{s}$, with an additional term to model the process of spin relaxation [34, 29],

$$\frac{\partial \vec{s}}{\partial t} = \frac{\partial \vec{J}_s}{\partial x} - \frac{\vec{s}}{\tau_s}, \tag{69}$$

where the spin current, $\vec{I}_s$, is due to both drift and diffusion currents,

$$\vec{J}_s = \mu E \vec{s} + D \frac{\partial \vec{s}}{\partial x}. \tag{70}$$

The scalar components of the spin accumulation is a function of the spin quasi-chemical potential, μ_s , and the density of states,

$$s_i = \mu_{s,i} \frac{\partial n_0}{\partial \eta}, \tag{71}$$

where, η, is the chemical potential and n_0 is the carrier concentration. Substituting μ_s into (71) and then dividing by V_s,

$$\begin{aligned} s_i &= V_{s,i} q^2 \frac{\partial n_0}{\partial \eta} \\ \frac{s_i}{V_{s,i}} &= q^2 \frac{\partial n_0}{\partial \eta} \equiv C_q, \end{aligned} \tag{72}$$

where we have recognized the result as C_q, the quantum capacitance per unit volume.

If we invoke Einstein's relation $\sigma = q^2 D \frac{\partial n_0}{\partial \eta}$ we can write the quantum capacitance as $C_q = \frac{\sigma}{D}$. We can also substitute the spin accumulation, $\vec{s}$, for the spin voltage, $\vec{V}_s$ as they

are directly proportional, $\vec{s} = \frac{\sigma}{qD}\vec{V}_s$. Substituting into (69) & (70) and using the tensor representations for $\overline{I}_s$ and $\overline{V}_s$ we are left with,

$$\begin{aligned} \mathbf{C}_s \frac{\partial \overline{V}_s}{\partial t} &= \frac{\partial \overline{I}_s}{\partial x} - \mathbf{G}_s \overline{V}_s, \\ \overline{I}_s &= \sigma A \frac{\partial \overline{V}_s}{\partial x} + \frac{\mu I_C}{D} \overline{V}_s, \end{aligned} \tag{73}$$

where $\mathbf{C}_s$ and $\mathbf{G}_s$ are the capacitance and conductance per unit length matrices defined as,

$$\begin{aligned} \mathbf{C}_s &= \begin{bmatrix} C_e & 0 & 0 & 0 \\ 0 & C_q A & 0 & 0 \\ 0 & 0 & C_q A & 0 \\ 0 & 0 & 0 & C_q A \end{bmatrix}, \\ \mathbf{G}_s &= \begin{bmatrix} 0 & 0 & 0 & 0 \\ 0 & \frac{C_q A}{\tau_s} & 0 & 0 \\ 0 & 0 & \frac{C_q A}{\tau_s} & 0 \\ 0 & 0 & 0 & \frac{C_q A}{\tau_s} \end{bmatrix}. \end{aligned} \tag{74}$$

where we have added the channel area, A, in order to express the equations in terms of the spin current, $\vec{I}_s$.

Simplifying the analysis of the drift-diffusion equations requires an approximation of the spatial derivative, ∂x. The finite-difference method is applied to the drift-diffusion equation to approximate a non-magnetic conductor of length L. The finite-difference approximation $\frac{\partial}{\partial x} \Rightarrow \frac{\Delta}{\Delta x}$ results in N number of drift-diffusion equations, each for a conductor segment of length $\Delta x = \frac{L}{N}$. The segments of length Δx cause a difference in voltage of $\Delta \overline{V}_s = \Delta \overline{V}_s(x) - \Delta \overline{V}_s(x + \Delta x)$ and a change in current of $\Delta \overline{I}_s = \Delta \overline{I}_s(x) - \Delta \overline{I}_s(x + \Delta x)$.

Each segment in a non-magnetic conductor is represented using a circuit model. The circuit model is derived by solving for $\overline{I}_s$ and $\Delta \overline{I}_s$. The complete circuit model for spin transport, Fig. 12 consists of cascaded segments for each component of the $\overline{V}_s$ and $\overline{I}_s$ tensors.

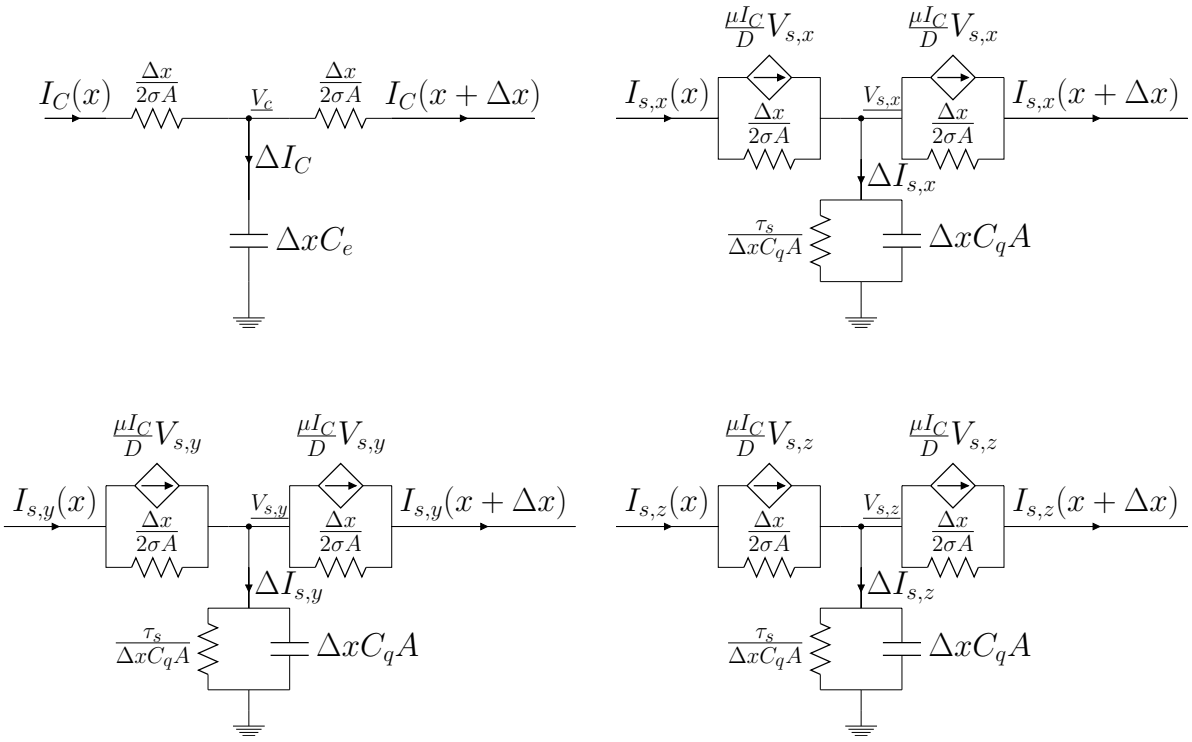

Figure 12: Equivalent Circuit Model for Spin Transport (Non-Magnetic Conductor of Length Δx).

3.3.1 Validation of Spin Drift-Diffusion

The spatial discretization is the key assumption that enables the development of the spin transport circuit model. The analytical solution of the steady-state case provides an accurate solution of the spatial propagation of the spin voltage [29], therefore making it a suitable formula for validating the finite-difference approximation used by the circuit model. In Fig. 13 the circuit simulations of the spin transport model accurately predict the spatial propagation of the spin voltage within 1% of the analytical solution for the steady-state case.

3.4 Circuit Model of All-Spin Logic

Using the circuit models that have been developed we are now able to completely describe a spintronic device using circuit elements. We will begin by simulating a family of spintronic devices known as All-Spin Logic (ASL) [6].

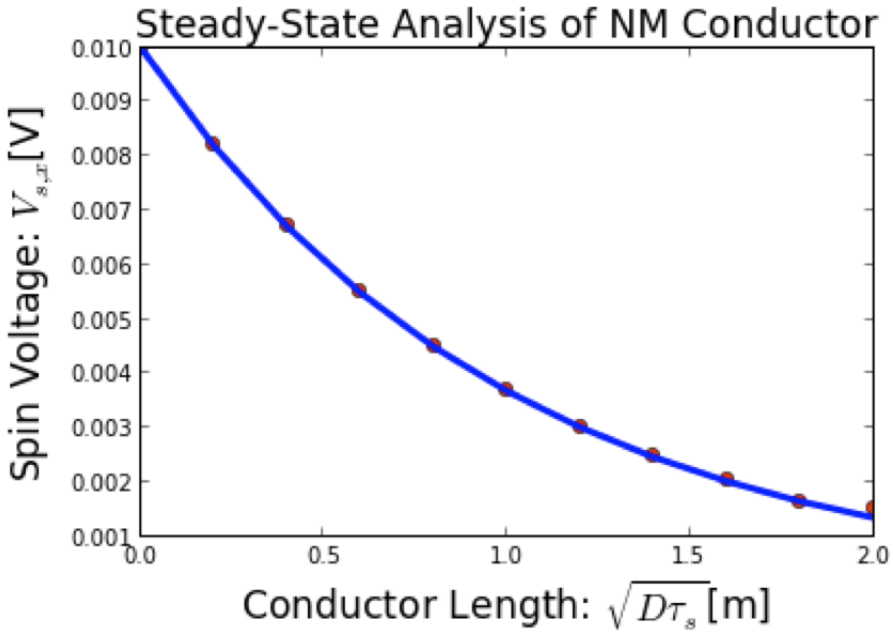

Figure 13: Non-magnetic Conductor Steady-State Analysis. Red symbols represent the circuit simulations while the blue curve shows the analytical solution. The x-axis represents the length relative to the spin diffusion length, $L_s = \sqrt{D\tau_s}$.

All-Spin Logic functions by storing the state of a boolean variable in the magnetization of an output ferromagnet. A non-magnetic conductor then connects the output ferromagnet to an input ferromagnet. The applied bias voltage determines the function of the device, where positive bias voltages cause the output ferromagnet to invert, while negative bias voltages cause the output ferromagnet to copy the state of the input ferromagnet. This mode of operation is what drives the first device device will study, a boolean logic inverter. We will then extend the ASL inverter into a majority gate capable of the NAND/NOR boolean logic functionality.

A simplified circuit model of an ASL device is shown in Fig. 14 which indicates the majority logic functionality that ASL devices are capable of performing. In this illustration, the capacitors represent the magnetizations of the ferromagnets present in ASL devices. The inverter represents the polarity of the logical operation performed, since for positive bias voltages ASL is complementary in nature. Each ferromagnet serves as an input logic

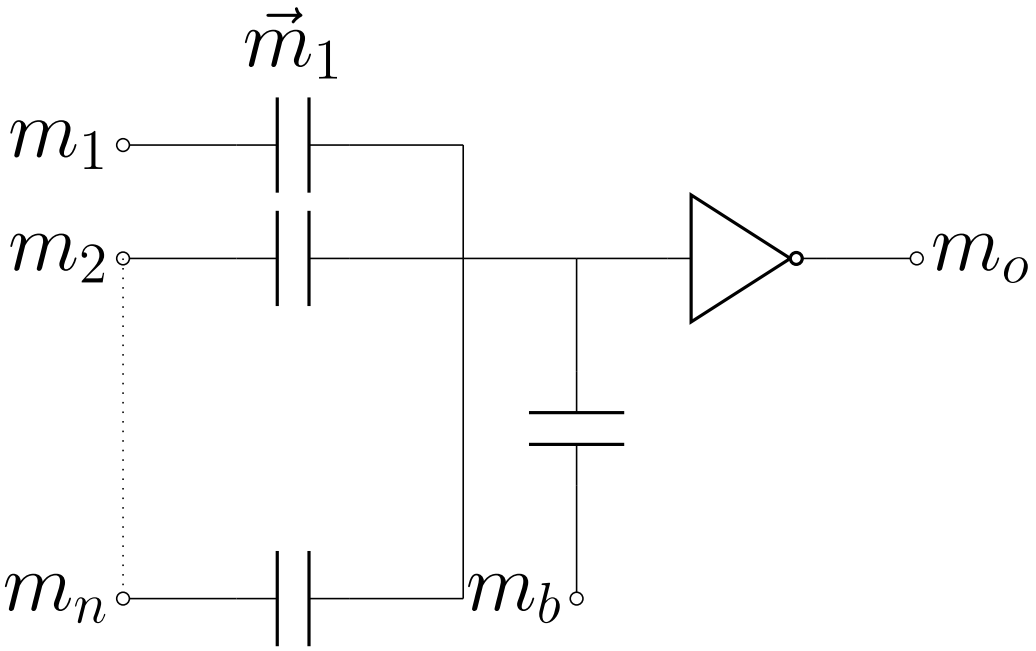

Figure 14: All-Spin Logic Device Behavior.

bit, with an additional ferromagnet used to bias the structure. We can think of this device as an N-input NAND/NOR logic gate, where the polarity of the magnet m_b determines whether the device behaves as either a NAND gate or a NOR gate.

First, we will look at the one input ASL inverter. The ASL inverter is constructed by connecting two ferromagnetic elements with a non-magnetic conducting channel. The input of the device is then formed by shunting an additional non-magnetic channel to ground close to the input ferromagnet. This is illustrated in Fig. 14, where we have only considered one stage of logic. The input and output ferromagnets can be connected to other ferromagnets using an isolation barrier. This enables the cascading of ASL stages that are capable of performing complex boolean logic functions. For now, we will only consider a single stage inverter.

The ASL inverter is biased by applying a voltage at the ferromagnet terminals. Qualitatively, the device functions by shunting all DC charge current from the input magnet into

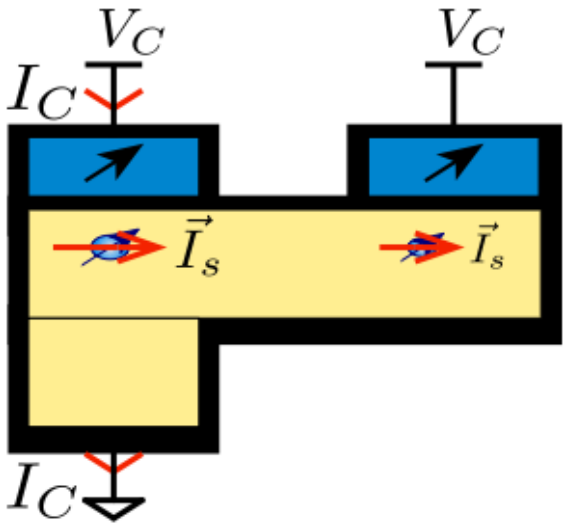

Figure 15: All-Spin Logic Inverter Illustration.

the ground channel. This is possible since the resistance between the input and output ferromagnets is small, thus minimizing the amount of charge current in the channel. Equation 29 predicts that in the collinear case, the spin current along the $\pm x$ direction at the FM/NM interface is,

$$I_{s,x} = V_{s,x}G_{\uparrow} + V_C G_{\downarrow}, \tag{75}$$

where $V_{s,x}$ is the spin voltage across the FM/NM interface. This tells us that the charge current will be coupled to the spin current through $G_{\downarrow}$, and therefore higher charge currents will result in higher spin currents along $\pm x$. This is significant since the charge current at the output ferromagnet is much lower than the charge current at the input ferromagnet ($I_{C,r} \gg I_{C,t}$). This results in spin current flowing from the transmitter to the receiver for positive bias voltages. We will present analytical equations later that demonstrate the relation between this bilateral operation and the material parameters of the ferromagnet, non-magnetic conductor, and the material interface.

The complete equivalent circuit for an ASL inverter is shown in Fig. 16, where we have combined the circuit models for spin storage, injection, and transport. An important point is that we consider the spin accumulation inside of the ferromagnet to be 0. This

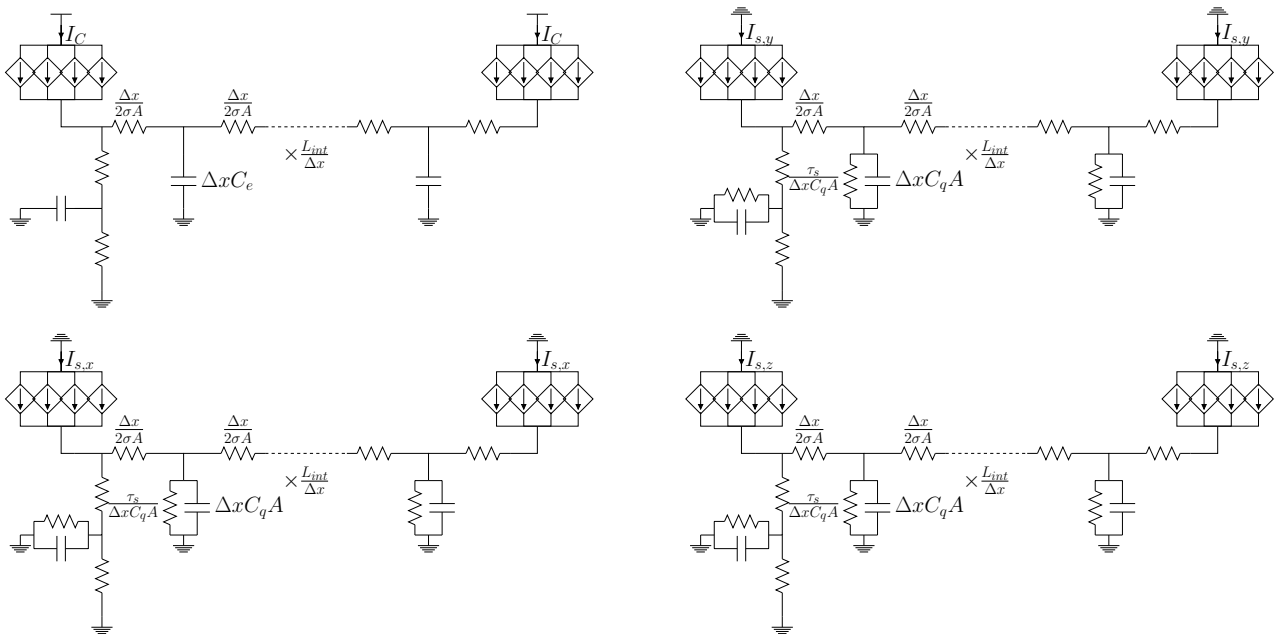

Figure 16: All-Spin Logic Inverter Schematic.

is represented by the grounds that are present on the ferromagnet side of the interface current sources. This is a reasonable approximation since the bias terminals are formed by connecting an additional non-magnetic conductor to the ferromagnet similar to the channel side of the interface, except the voltage on the bias side of the ferromagnet is kept at the supply, keeping the voltage drop to a minimum, thus minimizing the spin current according to Eq. 75.

The circuit model of Fig. 16 can be used to perform simulations of the ASL inverter. Previous works, [3, 35], have shown how ASL inverters perform under different bias voltages. In Fig. 17 an ASL device is driven by a 100 mV pulse. When the supply is +100 mV the device behaves as an inverter, and the output magnet switches to the opposite state of the input magnet. When the supply is −100 mV the output performs the opposite operation and copies the state of the input magnet.

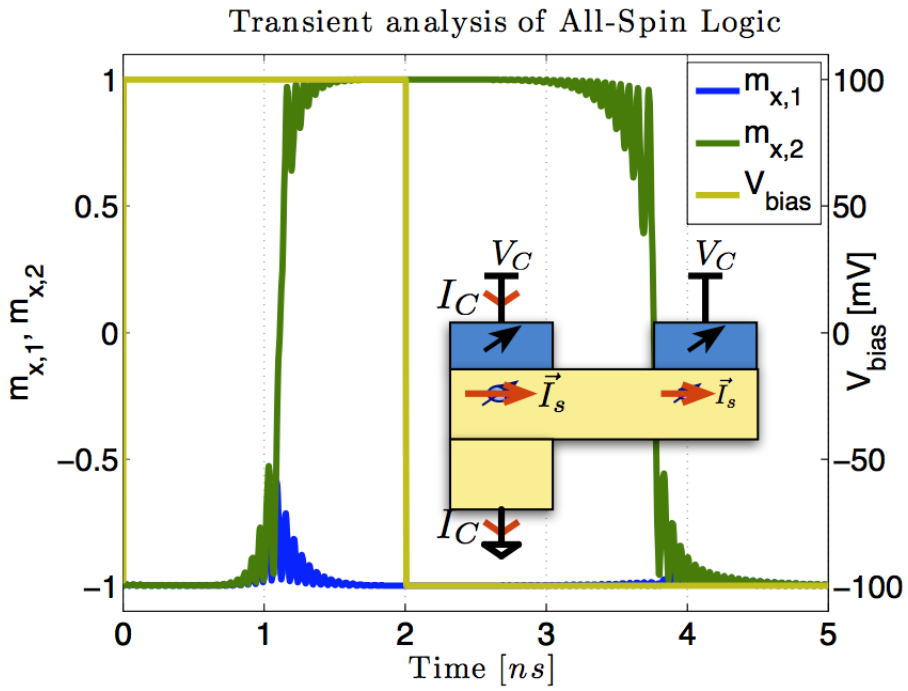

Figure 17: ASL Transient Analysis.

3.4.1 ASL Majority Gate

If we condsider the schematic shown in Fig. 14, we can utilize the models developed in this work to construct boolean logic devices that are capable of NAND and NOR logic operations, in addition to the invertering logic circuit shown in Fig. 15. This is accomplished by treating each input of the majority logic as an input ferromagnet, and constructing multiple interconnect and ground channels for each input. The channels are then connected to an output ferromagnet as shown in Fig. 18.

We have constructed a device that behaves as a majority gate capable of the boolean NAND and NOR operations. The magnets $\vec{m}_1$ and $\vec{m}_2$ serve as inputs while $\vec{m}_C$ is used to bias the device as a NAND or NOR gate. When the bias magnet is configured in the $-x$ direction, the device behaves as a NAND gate. When biased in the $+x$ direction the device functions as a NOR gate. The transient simulation of the ASL majority gate is shown in Fig. 19 for both the NAND and NOR functions.

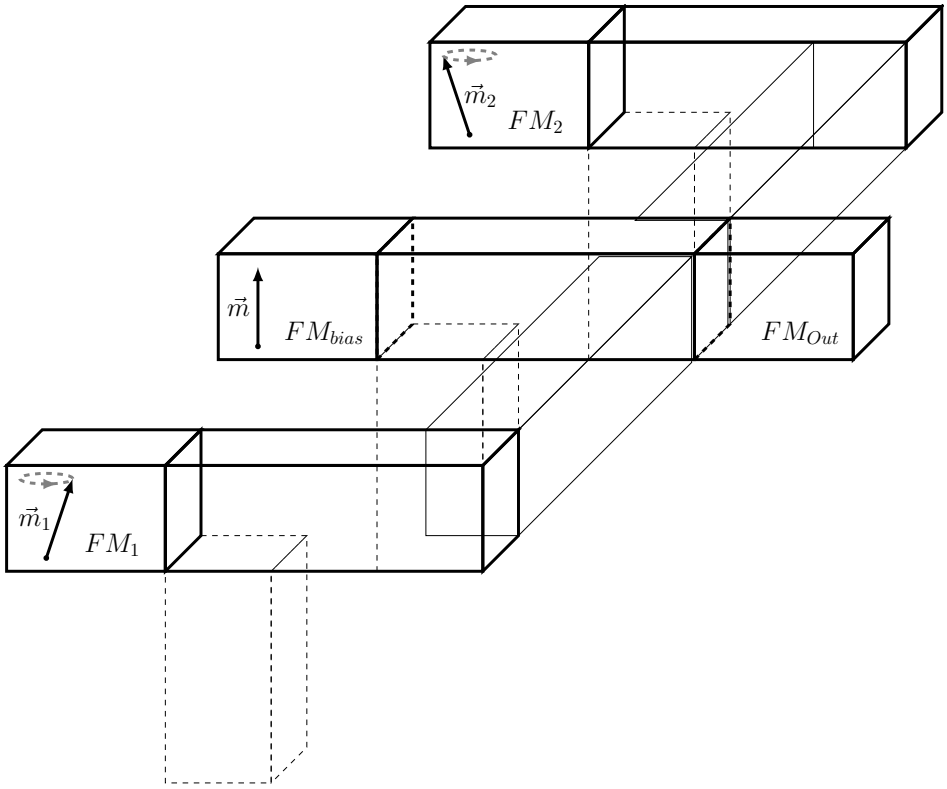

Figure 18: Majority Gate.

In Fig. 19 we have simulated the two input binary inputs of 00, 01, 10, and 11. The input magnets have been artificially switched using input spin current branches not illustrated in the schematics. An important aspect of designing with majority logic gates, is that the current produced from the bias magnet affects the switching characteristics of the device. This can be seen by looking at the input magnet, $\vec{m}_1$. The timing of the switching input is the same for both the NAND and NOR case, but $\vec{m}_1$ clearly switches differently for each case. This is due to the current produced in the bias magnet's channel, which causes a back injected current that affects the timing. In this case, the NAND simulation takes longer to switch from the $-x$ to $+x$ direction than the NOR case. However, the NAND simulation switches more quickly than the NOR when switching from $+x$ to $-x$.

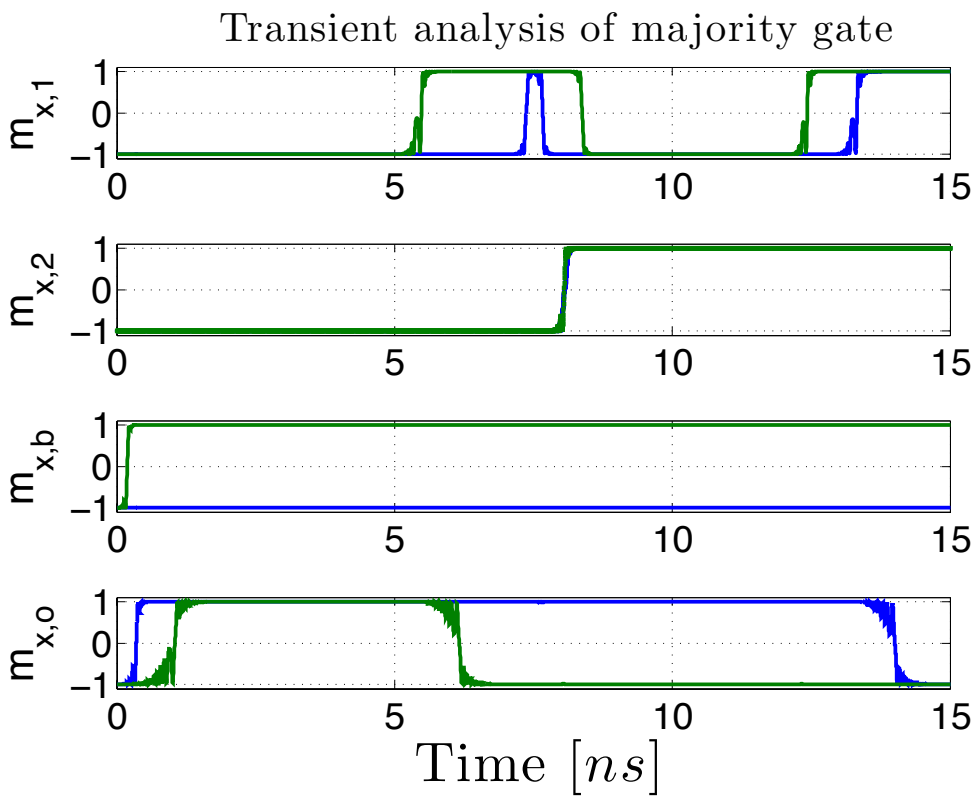

Figure 19: Majority Gate Transient Analysis (blue-NAND, green NOR).

3.5 Circuit Model of Spin-Hall Effect Switch

An additional spintronic device that is capable of Boolean logic operations is the Spin-Hall Effect Switch [2]. The compact circuit model for spin storage can be used to model the ferromagnetic elements in such a device. Figure. 20 shows a Spin-Hall Effect Switch, where a) is an illustration of the device, b) shows an equivalent circuit, and c) shows the characteristics of the output of such a device. The Spin-Hall Effect Switch behaves as a Boolean logic inverter and is composed of a Write circuit and a Read circuit.

The Write circuit works by exploiting the spin-hall effect [2] to induce a spin current in a ferromagnet. This spin current is generated by the factor β and is proportional to the current flowing through the resistor, r. The Read circuit functions by generating a current between the $V+$ and $V-$ terminals that is proportional to the dot product between the two fixed magnets and the Read magnet. The Write circuit is connected to the Read circuit through

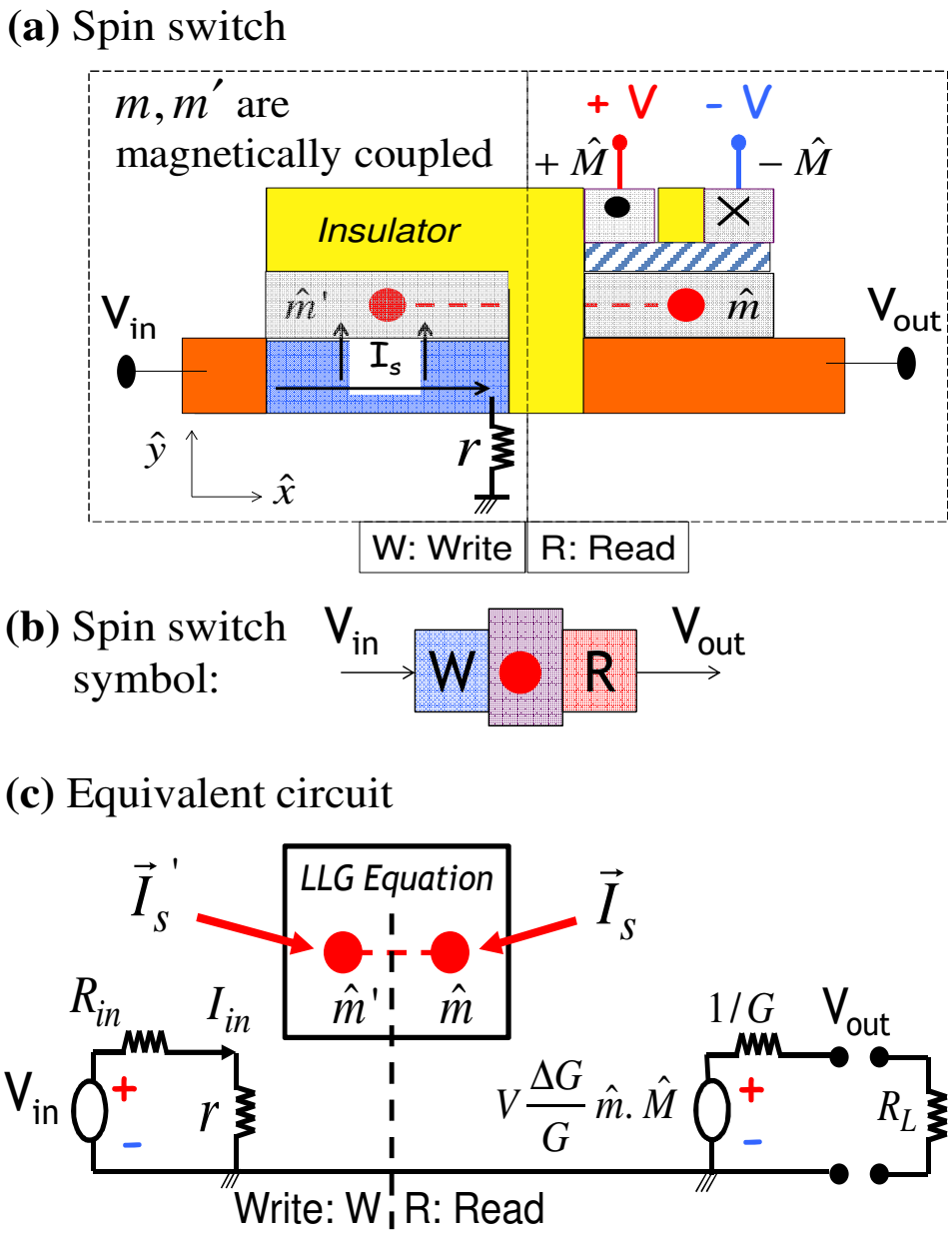

Figure 20: Spin-Hall Effect Switch: a) Illustration b) Equivalent Circuit c) Inverter Transfer Curve (Image Source [2]).

the dipolar coupling between the electrically isolated Write and Read ferromagnets.

We have created a compact model of the Spin-Hall Effect switch based on the circuit model developed for Spin Storage. Figure 21 shows the transient analysis in SPICE of the Spin-Hall Effect Switch. This demonstrates how the models developed in this work can be applied to other spintronic devices.

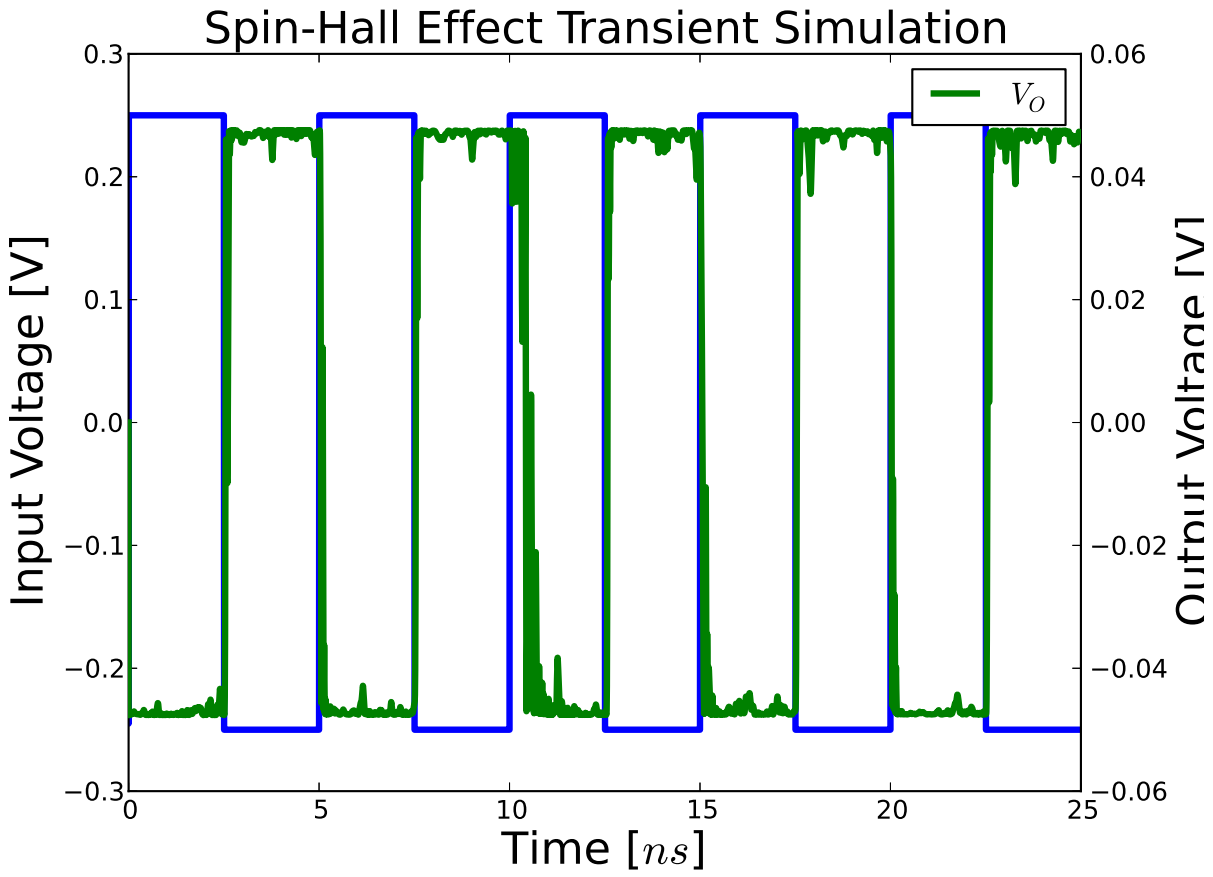

Figure 21: Transient Analysis of Spin-Hall Effect Inverter.

CHAPTER 4

DISCUSSION OF SPINTRONIC CIRCUIT MODELS

The circuit models developed in this work enable circuit designers to simulate and analyze a variety of spintronic devices. Although limited by the assumptions inherent in the physical equations, there are other issues present in the simulation and analysis of the various devices present. We will start by discussing an analysis that has been performed on All-Spin Logic devices in order to explain their operation and provide guidance for their design. Simulation results will also be presented that show limitations of the models developed in this work.

4.1 Analytical Equations for ASL Device Performance

4.1.1 ASL Performance Modeling - Equivalent Circuit

By re-examining the equivalent circuit of the ASL inverter shown in Fig. 16, we will derive analytical equations that demonstrate the performance characteristics of All-Spin Logic devices. These equations will be useful to circuit designers who need to leverage spintronic devices into integrated circuits.

We begin by noting that in digital applications we are interested in storing the state variable bit in the magnetization of the ferromagnet. For reference, we will be using the $\pm x$ direction to encode the logic 1 and logic 0 states, respectively. We will therefore simplify our circuit model in order to derive useful analytical equations. We begin by looking at the interface model in the collinear case, the spin current is found to be,

$$\begin{bmatrix} I_C \\ I_{s,x} \\ I_{s,y} \\ I_{s,z} \end{bmatrix} = \begin{bmatrix} G_\uparrow & G_\downarrow & 0 & 0 \\ G_\downarrow & G_\uparrow & 0 & 0 \\ 0 & 0 & 2\mathrm{Re}G_{\uparrow\downarrow} & 2\mathrm{Im}G_{\uparrow\downarrow} \\ 0 & 0 & -2\mathrm{Im}G_{\uparrow\downarrow} & 2\mathrm{Re}G_{\uparrow\downarrow} \end{bmatrix} \begin{bmatrix} V_{C,F} - V_{C,N} \\ -V_{s,x} \\ -V_{s,y} \\ -V_{s,z} \end{bmatrix}. \tag{76}$$

Under the assumption that $G_\uparrow \gg G_\downarrow$,

$$\begin{bmatrix} I_C \\ I_{s,x} \\ I_{s,y} \\ I_{s,z} \end{bmatrix} = \begin{bmatrix} V_C G_\uparrow \\ V_{s,x} G_\uparrow + V_C G_\downarrow \\ 0 \\ 0 \end{bmatrix}, \tag{77}$$

for $\vec{m}_1 = \vec{m}_2$. For $\vec{m}_1 = -\vec{m}_2$,

$$\begin{bmatrix} I_C \\ I_{s,x} \\ I_{s,y} \\ I_{s,z} \end{bmatrix} = \begin{bmatrix} G_\uparrow & -G_\downarrow & 0 & 0 \\ -G_\downarrow & G_\uparrow & 0 & 0 \\ 0 & 0 & 2\mathrm{Re}G_{\uparrow\downarrow} & 2\mathrm{Im}G_{\uparrow\downarrow} \\ 0 & 0 & -2\mathrm{Im}G_{\uparrow\downarrow} & 2\mathrm{Re}G_{\uparrow\downarrow} \end{bmatrix} \begin{bmatrix} V_{C,F} - V_{C,N} \\ -V_{s,x} \\ -V_{s,y} \\ -V_{s,z} \end{bmatrix}. \tag{78}$$

Again assuming that $G_\uparrow \gg G_\downarrow$,

$$\begin{bmatrix} I_C \\ I_{s,x} \\ I_{s,y} \\ I_{s,z} \end{bmatrix} = \begin{bmatrix} V_C G_\uparrow \\ V_{s,x} G_\uparrow - V_C G_\downarrow \\ 0 \\ 0 \end{bmatrix}. \tag{79}$$

If we make an additional assumption about the non-magnetic conductor channels, then we can simplify the ASL circuit even further. We will do this by considering the conductor length to be $L_{int} = \Delta x$, which assumes that the non-magnetic conductor circuit consists of only one segment length. Due to the 0 spin currents generated in $I_{s,y}$ and $I_{s,z}$, we will only consider two separate current quantities, I_C and $I_{s,x}$. Combining this with the simplification made earlier about the spin current at the interface results in the equivalent circuit for the ASL inverter as shown in Fig. 22. This equivalent circuit models a good approximation of the non-magnetic conductor and interface under conditions which the magnetizations are collinear. We can therefore derive properties of the channel and interface and develop design optimizations for ASL devices. It is important to note that we have assumed that the ground channel length is equal to the channel length that separates the ferromagnets.

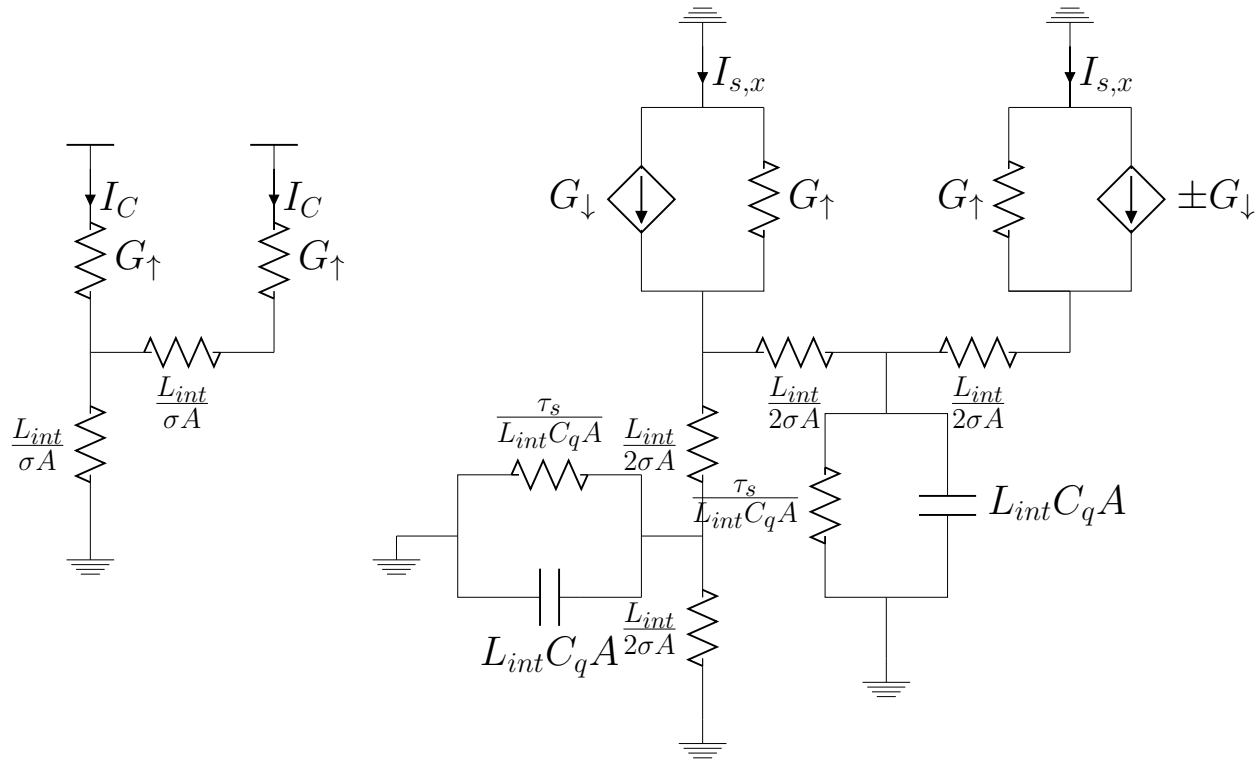

Figure 22: Equivalent circuit for ASL Inverter assuming collinear approximation.

This assumption is only invalid for very short, $L_{int} \leq$ 50nm channels or very long, $L_{int} \leq$ 5000nm channels. At very short ground channel lengths, most of the spin current from the transmitter is shunted to ground, while at very long channel lengths the series resistance of the ground channel is too high for spin injection from the transmitter to occur. We have also neglected the effect of the shunt capacitances in the following derivations.

If we solve the spin path for the transmitter and receiver spin currents, we can design a device to maximize the efficiency (loss) of spin transport, $\frac{I_{s,r}}{I_{s,t}}$. We will call this parameter β_s and it represents the ability of the ASL device to transport spin from the transmitter to the receiver. For now we will assume that the length of the ground channel, $S_{gnd} = 1$. Performing nodal analysis on the spin path results in,

$$\beta_{s,\parallel} = \frac{10G_\uparrow^2 L_s^2 S_{int} - 5AG_\uparrow L_s \sigma S_{int}^2 - 2A^2\sigma^2\left(6 + 5S_{int} + 3S_{int}^2\right)}{2A^2\sigma^2\left(6 + 5S_{int} + 3S_{int}^2\right) + 3AG_\uparrow L_s \sigma S_{int}\left(8 + 5S_{int} + 3S_{int}^2\right) + G_\uparrow^2 L_s^2 S_{int}\left(10 + 12S_{int} + 5S_{int}^2 + 3S_{int}^3\right)} \tag{80}$$

and,

$$\beta_{s,-\|} = \frac{10G_{\uparrow}^2 L_s^2 S_{int} + 5AG_{\uparrow}L_s\sigma\left(4 + S_{int}^2\right) + 2A^2\sigma^2\left(6 + 5S_{int} + 3S_{int}^2\right)}{G_{\uparrow}^2 L_s^2 S_{int}\left(10 + 12S_{int} + 5S_{int}^2 + 3S_{int}^3\right) + AG_{\uparrow}L_s\sigma\left(20 + 24S_{int} + 15S_{int}^2 + 9S_{int}^3\right)}. \tag{81}$$

The formula for $\beta_{s,\|}$ exhibits a local maximum for the parameter ranges that we are interested in. However, the maximum cannot be solved analytically in terms of the present parameters since it involves finding the root of a quintic polynomial. Instead, we will examine the results numerically and derive general assumptions about the transfer of spin polarized current in All-Spin Logic devices.

Assuming the standard parameters (See Appendix A) for an ASL device with Cobalt ferromagnets and a Copper channel with $S_{gnd} = 1$, we can plot the dependence of the spin loss on the channel length, $\beta_s(S_{int})$ as shown in Fig. 23. The spin loss, β_s, exhibits a local maximum that suggests an optimal channel length for ASL device designs. Figure 23 shows the channel length that results in the maximum spin loss. The result has been found numerically and occurs at approximately $L_{int} = 0.172_s$ and results in a spin loss of 0.52. If given the challenge of choosing a desirable channel length for ASL, then β_s provides us with valuable insight. At short channel lengths, the back-injected current begins to have a noticeable impact on device performance.

4.1.2 Ferromagnet Delay

We will design the ferromagnet by examining two key equations based off of the model derived in [33] for ferromagnets with uniaxial anisotropy. This model is based off of the Stoner-Wohlfarth model and assumes spin-transfer torque switching in a rectangular ferromagnet that is square along x and y with length, a. Along the z direction the length, L_z, is assumed to be much less than a ($L_z \ll a$). Small cone-angles ($\theta \ll 1$) are used to simplify the LLG equation and derive analytical expressions related to spin transfer torque switching in ferromagnets. The first equations predicts the minimum threshold current that

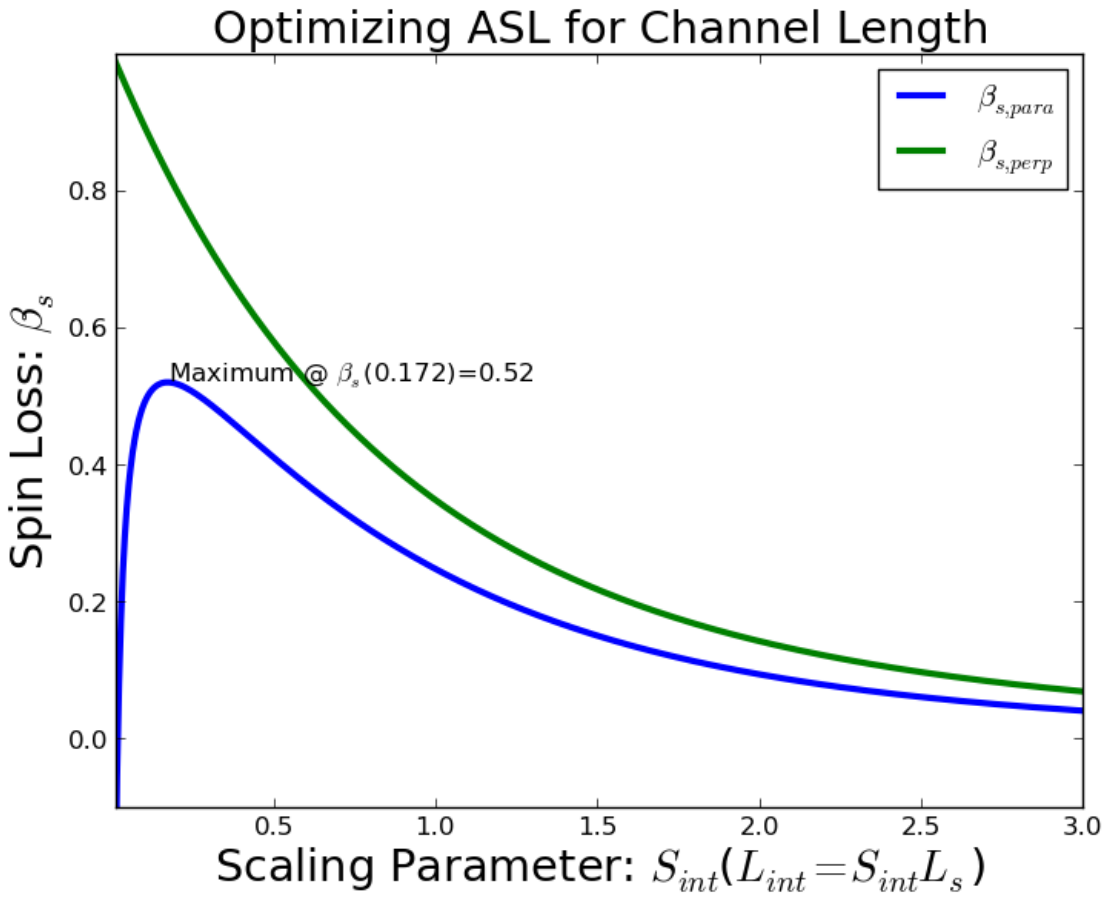

Figure 23: Spin Loss, β_s, of an ASL inverter as a function of the channel length. The local extrema for the parallel case occurs at $S_{int} = 0.172$.

induces spin-transfer torque switching, $I_{s,cr}$, which is found to be,

$$I_{s,cr} = \frac{4q}{\hbar|\cos\phi|}\alpha V\left(K + M_s^2\pi\right). \tag{82}$$

It is clear that the critical switching current varies linearly with the Volume, $V = L_xL_yL_z$, the Gilbert damping parameter, α, and the anisotropy constant, K. The cricital switching current varies quadratically with the saturation magnetization, M_s.

The volume is determined by the layout of the device, and will be a parameter adjustable by design engineers. It is clear that magnets with smaller volumes are easier to switch, due to the fact that they require smaller currents to ensure successful switching. The minimum magnet dimensions will be limited by the process lithography's features sizes. We will also

demonstrate that decreasing the magnet volume leads to a greater susceptibility to thermal noise, placing another practical limit on how small the ferromagnets may be sized as part of a circuit design.

The parameters, α, K, and M_s are determined by the ferromagnetic material properties. We stated in Eq. 82 that the critical current increases linearly with α and K, while increasing quadratically with M_s. Ref. [22] shows a table of values for the ferromagnet material parameters for Iron, Cobalt, Nickel, and Permalloy. The damping parameter, α, is relatively constant for different ferromagnetic materials ($0.007 - 0.01$). The choice of material therefore depends on the magnitudes of the anisotropy energy constant, K, and the saturation magnetization, M_s. The magnitude of the anisotropy constant varies from approximately 0 to 5×10^5, and is actually negative in Nickel. The saturation magnetization varies from 0.485×10^6 in Nickel to 1.71×10^6 in Iron. Though not as significant a variation, the critical current increases quadratically with M_s according to Eq. 82, so a careful choice must be made to balance the benefits of reduced M_s with the change in K that is present in a different material.

The second equation predicts the switching time for a spin-transfer torque oscillation, and will be useful in predicting the performance characteristics of ASL devices. This derivation is also based on square ferromagnets with uniaxial anisotropy as shown in [33]. The equation for the switching time is,

$$\tau_{sw} = \frac{M_s V q}{I_{s,cr} \mu_b} \frac{\log \pi/\theta_0}{\chi - 1}. \tag{83}$$

where χ is a parameter that we will use to design ASL devices. Ferromagnets will not switch states for $\chi \leq 1$, and this will serve as an important determination of the supply voltage limits present in ASL devices. In the case of delay, the delay decreases inversely proportionally to the applied current, $I_{s,x} = \chi I_{s,cr}$. The applied spin current will depend on the circuit topology and the value of β_s that we have previously shown how to optimize for. The delay increases linearly with both the volume, V, and the saturation magnetization, M_s. Since the critical spin current, $I_{s,cr}$, suggests that we aim for minimal V and M_s in our

ASL parameters, the delay does not introduce any additional constraints on our ASL circuit design.

4.1.3 Simulation Results

Since we are ultimately using the β_s factor to measure efficiency of spin transferred from the transmitter of an ASL device to the receiver, we will show the delay of an ASL device versus channel length. We have already looked at the effect of channel length versus the spin current lost in a non-magnetic conductor (Fig. 6). This clearly demonstrated that longer channel lengths result in a loss of spin current, but in the context of ASL devices, the β_s factor is the figure of merit that we seek to use to discern the effect of varying channel lengths. We will use the SPICE simulations to show the delay as a function of channel length in order to validate formulas 80 & 81.

Figure 24 shows the delay as a function of channel length for an ASL device under parallel switching conditions. In this simulation the delay increases monotically over the entire range that we have simulated. This opposes our intuition developed in Eq. 80 which suggested that there is an optimal channel length for the best efficiency of transmitted spin current across the device channel.

To investigate this, we will verify that the expressions themself are correct in computing the value of β_s for a given ASL device channel. Figure 25 shows the value of beta calculated for the parallel switching case. This matches well with the analytical results shown in Fig. 23. We anticipate that the perpendicular results will match well, since the key assumption that we have made about the collinear model holds for both cases.

We must still rectify the difference between the local maximum exhibited in both the analytical results and the simulations for β_s. Higher β_s results in higher receiver spin currents, independent of supply voltage. We therefore expect that at higher spin currents the switching time is decreased and follows the trend predicted by Eq. 83.

In an attempt to explain this difference between the simulation results for the delay and the conclusions that we drew from our understanding of the analytical expressions, we

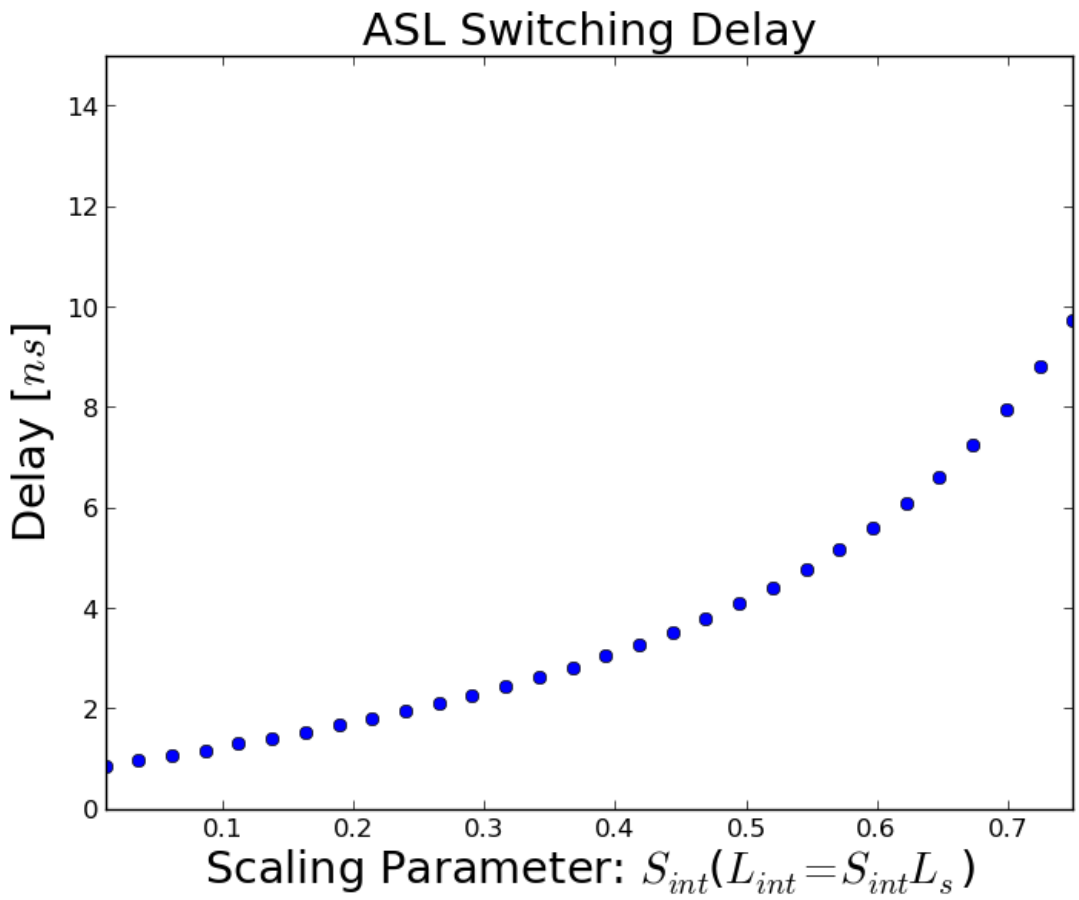

Figure 24: All-Spin Logic Device Delay (parallel switching) as a function of the channel length.

replaced the input ferromagnet with a fixed magnet that has a permanent magnetization of $\vec{m}_1 = +x$. This was done in an attempt to see if the small-cone angle approximation used in [33] still holds valid for All-Spin Logic devices. Since the input ferromagnet's magnetization does not remain constant (blue curve of Fig. 17), we can attempt to force the input spin current to be of a constant magnitude by using an input magnet of a constant magnetization.

The results are shown in Fig. 26, where the input magnetization is constant for the entire circuit simulation. Here, the delay exhibits a local minimum at approximately the same

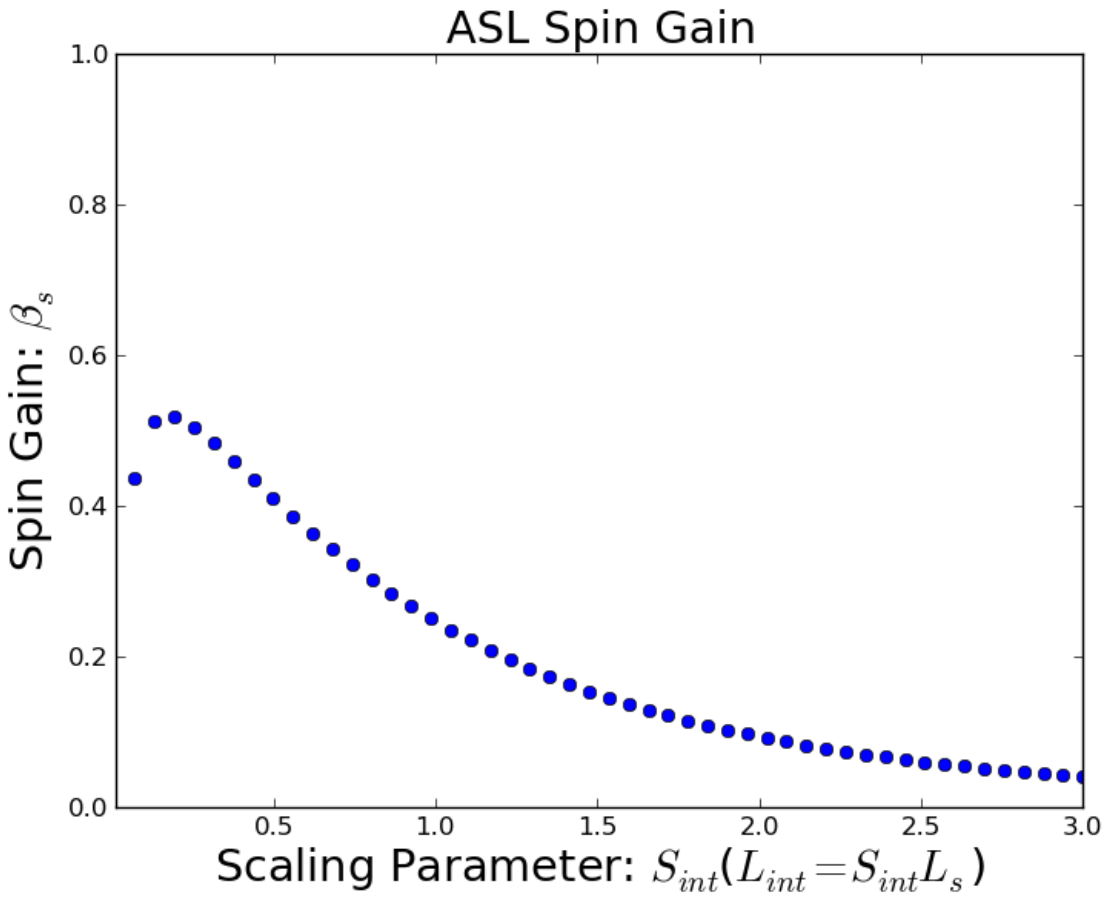

Figure 25: All-Spin Logic Device Spin Loss (parallel switching) as a function of the channel length using SPICE simulations.

length (S_{int} = 0.172) as shown in Fig. 23. This result stresses a key limitation of the small-cone angle assumption that is used to derive Eq. 83. The small-cone angle assumption does not hold in All-Spin Logic devices, since the imperfect unilateral transfer of spins causes a small procession in the input ferromagnet. Figure 17 illustrates this procession, and our model allows us to replace the input ferromagnet with a fixed magnet designed to illustrate the limitation of the small-cone angle approximation. When the fixed magnet is inserted, there is no procession of the input magnet, and therefore the transported current is of a constant magnitude that closely follows the assumptions presented in [33]. This is not realistic, and as such, great care must be taken when using the formulas developed in [33]

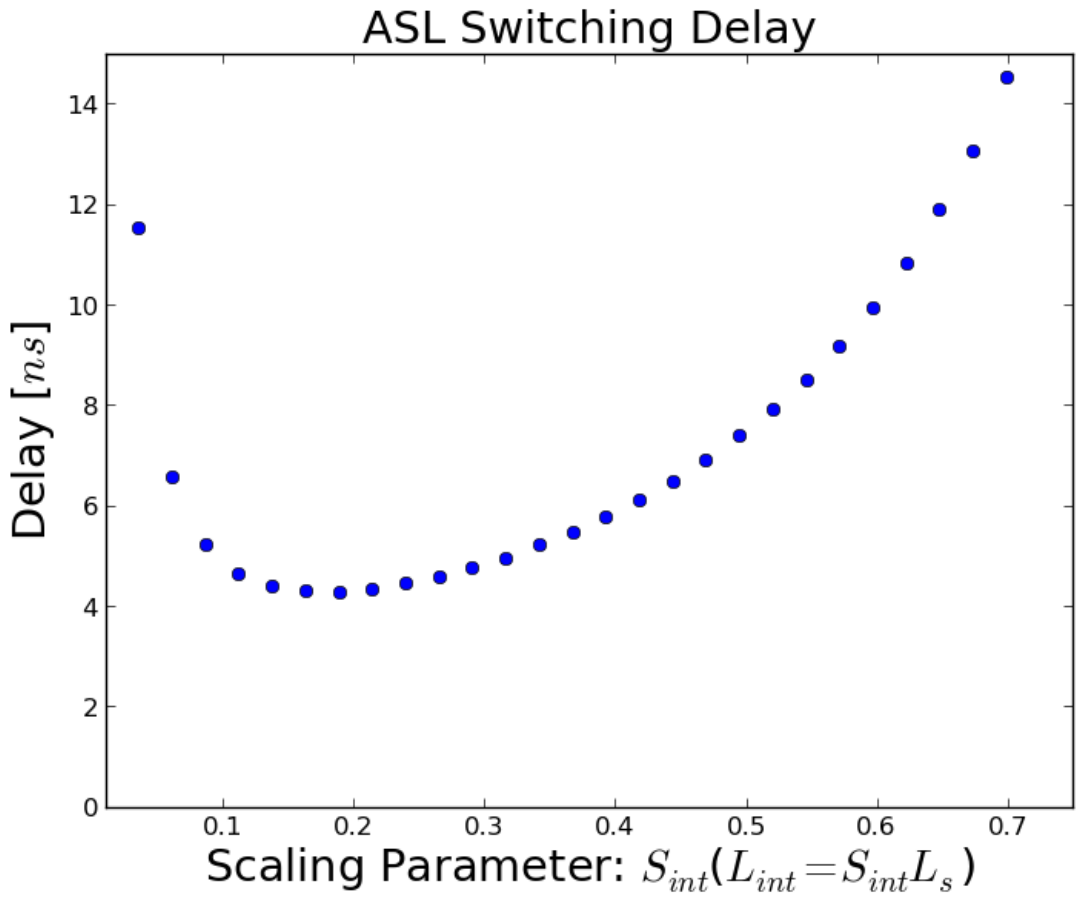

Figure 26: All-Spin Logic Device Delay (parallel switching) as a function of the channel length.

to predict ASL device performance.

4.2 Device Simulation

In addition to the analysis performed earlier, there are other aspects of the spintronic circuit models that warrant discussion. We will discuss issues that affect both the overall simulation time that is important in determining the overall simulation time of the models developed in this work, and some insight into how the model can be simplified in order to reduce this simulation time.

4.2.1 LLG Equation Stiffness

The LLG equation exhibits stiffness when the applied spin current, $\chi I_{s,cr}$, is close to the critical switching current, $I_{s,cr}$. When the applied current is $1.025I_{s,cr}$ a time step of 0.5 fs must be used in order to successfully simulate a switching event. When the applied current is increased to $1.25I_{s,cr}$ a larger time step of 5.0 fs can be used instead. The decrease in time step for lower spin currents leads to an increase in simulation time that is significant when performing circuit simulations. This has implications for simulations where ASL devices are operated at very low supply voltages. If successful results must be guaranteed, then initial simulations of a design should be performed at small time steps, provided that the spin currents are known from the analytical equations presented in this work.

4.2.2 Time Scale Comparison

When examining the delay of the ASL device, it became apparent that the delay is dominated by the switching dynamics of the ferromagnet. This can be observed by comparing the switching characteristics of the channel with the switching characteristics presented earlier for the ferromagnet. In order to do this, we simulated the structure shown in the inset of Fig. 27, where the spin current is measured at the end of the non-magnetic conductor. The delay between the magnet switching and the change in spin current after it traverses the channel was smaller than the time step of $0.4fs$ used in the simulation. This is significantly smaller than the switching delay of the ferromagnet, which was approximately 1 ns.

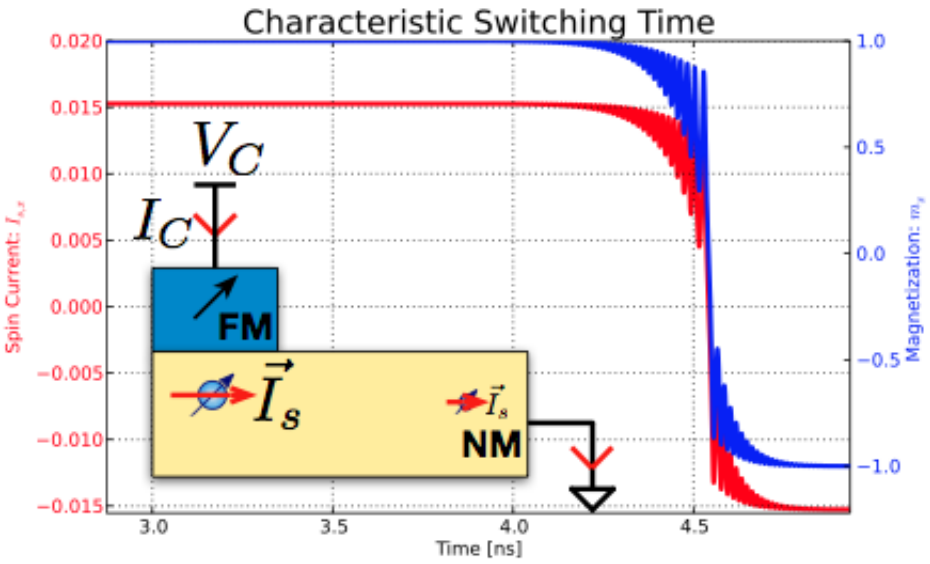

Figure 27: Ferromagnet & Channel Transient Analysis.

CHAPTER 5
SUMMARY AND OUTLOOK

In the interest of developing a novel technique for the simultaneous simulation of the magnetization dynamics of ferromagnets with the spin transport physics of non-magnetic conductors, we have developed new compact circuit models. In Chapter 2, circuit models for spintronic devices simulate the physics of spin transport in non-magnetic channels, spin storage in ferromagnetic elements, and spin injection that occurs at the material interface. In Chapter 3 we have derived equations that models these effects, and then mapped the physical equations to circuit elements. These circuit elements, along with the physical parameters, are used in a SPICE netlist to perform circuit simulations of spintronic devices. These simulations are compared to analytical solutions of the different physical systems in order to validate the compact models that have been developed. These models enable the co-simulation of the magnetization dynamics and spin transport physics necessary to simulate spintronic devices.

The spintronic devices that were examined in Chapter 3 show how the compact circuit models can be applied to simulating spintronic devices. The All-Spin Logic inverter and majority gates show an application for spintronic devices in digital logic applications. The recent inclusion of the Spin-Hall Effect Switch demonstrates how the ferromagnet model for the magnetization dynamics can be applied to other devices. We have also shown how a digital sense amplifier and an analog signal amplifier can be build from ferromagnets and non-magnetic conducting channels.

Additionally, we have shown how the collinear approximation can be used to derive a new equivalent circuit that is useful when designing All-Spin Logic devices. This equivalent circuit allows us to understand the performance of All-Spin Logic by expressing, for instance, the delay and power dissipation as a function of the channel, ferromagnet, and interface parameters. This enables the study of ASL devices using circuit design tools

and is essential to the design process of future spintronic devices. Preliminary work has shown that while these models are accurate for predicting the power dissipation and current magnitudes, there is still uncertainty in how the small-cone angle approximations will perform when the different compact models are combined in order to simulate ASL devices. Future work would involve validating the analytical equations and testing that the collinear approximation provides a sufficiently accurate model for predicting ASL device performance.

While the compact circuit models have proven to be accurate in simulating their respective physical systems, there are still limitations that device and circuit designers must be aware of when performing simulations of spintronic devices. The stiffness of the LLG equation can be particularly troublesome, since circuit simulators such as SPICE will continue to solve the system, although with inaccurate results if the time step of the simulation is not sufficiently small. In the end, the models developed in this work enable the study of spintronics using circuit design tools and is essential to the design process of future spintronic devices.

CHAPTER 6

APPENDICES

The following list includes all of the necessary parameters for the compact models presented in this paper. The interface parameters include the two-channel conductances, $G_{\uparrow}$ and $G_{\downarrow}$, and the mixing conductance, $G_{\uparrow\downarrow}$. The ferromagnet parameters include the dimensions, L_x, L_y, and L_z, the saturation magnetization, M_s, and the Gilbert Damping coefficient, α. The remaining ferromagnet parameters are a function of these, and we have referenced the relevant works for their calculation in the case of a Cobalt ferromagnet. The channel parameters include the dimensions, length (L_{int}), width (W_{int}), and the thickness to width aspect ratio (AR), in addition to the material parameters calculated in [30] for a Copper channel.

Interface Parameters(Co/Cu)[16]: $G_{\uparrow}$=0.600 $\frac{1}{\Omega}$, $G_{\downarrow}$=0.514 $\frac{1}{\Omega}$, Re$G_{\uparrow\downarrow}$=1.717 $\frac{1}{\Omega}$, Im$G_{\uparrow\downarrow}$=0.025 $\frac{1}{\Omega}$,

Ferromagnet(Co)[23, 24]: L_x=75.60 nm, L_y=37.80 nm, L_z=3.00 nm, α=0.01 -, γ=17.60 $\times$ 10^{10} $\frac{1}{sT}$, M_s=1.45 $\times$ 10^{06} $\frac{A}{m}$, N_s=1.34 $\times$ 10^{06} -, $\frac{1}{(1V)}N_s q(1+\alpha^2)$=214.72 fF, K_u=0.5 $\times$ 10^5 $\frac{J}{m^2}$, N_x=0.044 -, N_y=0.091 -, N_z=0.864 -,

Channel(Cu)[30]: L_{int}=100.0 nm, W_{int}=100.0 nm, AR=2.0 -, H_{int} = $\frac{W_{int}}{AR}$=50.0 nm, A = $W_{int}H_{int}$=5000.0 nm^2, Δx=10.0 nm, σ=41.549 $\frac{1}{\mu\Omega m^2}$, D=0.014 $\frac{m^2}{s}$, μ=0.003 $\frac{m^2}{Vs}$, τ_s=10.939 ps, R_s = $\frac{\Delta x}{2\sigma A}$=0.024 Ω, $R_{s,shunt}$ = $\frac{D\tau_s}{\sigma A\Delta x}$=74.982 Ω, C_s = $\frac{\sigma A\Delta x}{D}$=145.890 fF.

REFERENCES

[1] C. Kittel, "Theory of the structure of ferromagnetic domains in films and small particles," *Physical Review*, vol. 70, no. 11-12, p. 965, 1946.

[2] S. Datta, S. Salahuddin, and B. Behin-Aein, "Non-volatile spin switch for boolean and non-boolean logic," *Applied Physics Letters*, vol. 101, no. 25, pp. –, 2012.

[3] S. Srinivasan, A. Sarkar, B. Behin-Aein, and S. Datta, "All-Spin Logic Device With Inbuilt Nonreciprocity," *IEEE Transactions on Magnetics*, vol. 47, pp. 4026–4032, Oct. 2011.

[4] I. Žutić, J. Fabian, and S. Das Sarma, "Spintronics: Fundamentals and applications," *Rev. Mod. Phys.*, vol. 76, pp. 323–410, Apr 2004.

[5] J. Slonczewski, "Current-driven excitation of magnetic multilayers," *Journal of Magnetism and Magnetic Materials*, vol. 159, no. 12, pp. L1 – L7, 1996.

[6] B. Behin-Aein, D. Datta, S. Salahuddin, and S. Datta, "Proposal for an all-spin logic device with built-in memory," *Nature nanotechnology*, vol. 5, no. 4, pp. 266–270, 2010.

[7] E. I. Rashba, "Theory of electrical spin injection: Tunnel contacts as a solution of the conductivity mismatch problem," *Phys. Rev. B*, vol. 62, pp. R16267–R16270, Dec 2000.

[8] F. Mireles and G. Kirczenow, "From classical to quantum spintronics: Theory of coherent spin injection and spin valve phenomena," *EPL (Europhysics Letters)*, vol. 59, no. 1, p. 107, 2002.

[9] S. Das Sarma, J. Fabian, X. Hu, and I. Zutic, "Theoretical perspectives on spintronics and spin-polarized transport," *Magnetics, IEEE Transactions on*, vol. 36, no. 5, pp. 2821–2826, 2000.

[10] I. Zutic, J. Fabian, and S. Erwin, "Bipolar spintronics: Fundamentals and applications," *IBM Journal of Research and Development*, vol. 50, no. 1, pp. 121–139, 2006.

[11] L. Berger, "Emission of spin waves by a magnetic multilayer traversed by a current," *Phys. Rev. B*, vol. 54, pp. 9353–9358, Oct 1996.

[12] L. D. Landau and E. Lifshitz, "On the theory of the dispersion of magnetic permeability in ferromagnetic bodies," *Phys. Z. Sowjetunion*, vol. 8, no. 153, pp. 101–114, 1935.

[13] T. Gilbert and J. Kelly, "Anomalous rotational damping in ferromagnetic sheets," in *Conference on Magnetism and Magnetic Materials, Pittsburgh, PA*, pp. 253–263, 1955.

[14] T. Valet and A. Fert, "Theory of the perpendicular magnetoresistance in magnetic multilayers," *Phys. Rev. B*, vol. 48, pp. 7099–7113, Sep 1993.

[15] A. Brataas, Y. V. Nazarov, and G. E. W. Bauer, "Finite-Element Theory of Transport in Ferromagnet-Normal Metal Systems," *Physical Review Letters*, vol. 84, pp. 2481–2484, Mar. 2000.

[16] A. Brataas, G. E. Bauer, and P. J. Kelly, "Non-collinear magnetoelectronics," *Physics Reports*, vol. 427, no. 4, pp. 157 – 255, 2006.

[17] G. Panagopoulos and et al., "A framework for simulating hybrid mtj/cmos circuits: Atoms to system approach," in *Design, Automation Test in Europe Conference Exhibition (DATE), 2012*, pp. 1443–1446, 2012.

[18] B. Behin-Aein, A. Sarkar, S. Srinivasan, and S. Datta, "Switching energy-delay of all spin logic devices," *Applied Physics Letters*, vol. 98, no. 12, pp. –, 2011.

[19] T. Quarles, A. Newton, D. Pederson, and A. Sangiovanni-Vincentelli, "Spice 3 user manual," 1993.

[20] P. J. Cote and L. V. Meisel, "Self-organized criticality and the barkhausen effect," *Phys. Rev. Lett.*, vol. 67, pp. 1334–1337, Sep 1991.

[21] E. C. Stoner and E. Wohlfarth, "A mechanism of magnetic hysteresis in heterogeneous alloys," *Philosophical Transactions of the Royal Society of London. Series A. Mathematical and Physical Sciences*, pp. 599–642, 1948.

[22] C. Tannous and J. Gieraltowski, "The stonerwohlfarth model of ferromagnetism," *European Journal of Physics*, vol. 29, no. 3, p. 475, 2008.

[23] J. Xiao, A. Zangwill, and M. D. Stiles, "Macrospin models of spin transfer dynamics," *Phys. Rev. B*, vol. 72, p. 014446, Jul 2005.

[24] M. Beleggia, M. D. Graef, and Y. T. Millev, "The equivalent ellipsoid of a magnetized body," *Journal of Physics D: Applied Physics*, vol. 39, no. 5, p. 891, 2006.

[25] W. F. Brown Jr, "Thermal fluctuations of a single-domain particle," *Physical Review*, vol. 130, no. 5, p. 1677, 1963.

[26] M. C. Hickey and J. S. Moodera, "Origin of intrinsic gilbert damping," *Physical review letters*, vol. 102, no. 13, p. 137601, 2009.

[27] M. Stiles and A. Zangwill, "Anatomy of spin-transfer torque," *Physical Review B*, vol. 66, no. 1, p. 014407, 2002.

[28] S. Manipatruni, D. Nikonov, and I. Young, "Modeling and design of spintronic integrated circuits," *Circuits and Systems I: Regular Papers, IEEE Transactions on*, vol. 59, no. 12, pp. 2801–2814, 2012.

[29] J. Fabian, A. Matos-Abiague, C. Ertler, P. Stano, and I. Žutić, "Semiconductor spintronics," *Acta Physica Slovaca*, vol. 57, pp. 565–907, Aug. 2007.

[30] S. Rakheja, S.-C. Chang, and A. Naeemi, "Impact of dimensional scaling and size effects on spin transport in copper and aluminum interconnects," *Electron Devices, IEEE Transactions on*, vol. 60, no. 11, pp. 3913–3919, 2013.

[31] J. Brown, W., "Thermal fluctuation of fine ferromagnetic particles," *Magnetics, IEEE Transactions on*, vol. 15, no. 5, pp. 1196–1208, 1979.

[32] A. C. Hindmarsh, "ODEPACK, A Systematized Collection of ODE Solvers , R. S. Stepleman et al. (eds.), North-Holland, Amsterdam, (vol. 1 of), pp. 55-64.," *IMACS Transactions on Scientific Computation*, vol. 1, pp. 55–64, 1983.

[33] J. Z. Sun, "Spin-current interaction with a monodomain magnetic body: A model study," *Phys. Rev. B*, vol. 62, pp. 570–578, Jul 2000.

[34] J. Fabian and S. Das Sarma, "Spin relaxation of conduction electrons in polyvalent metals: Theory and a realistic calculation," *Phys. Rev. Lett.*, vol. 81, pp. 5624–5627, Dec 1998.

[35] B. Behin-Aein and S. Datta, "All-spin logic," in *Device Research Conference (DRC), 2010*, pp. 41–42, 2010.